

**Chapter 10: Global Climate Projections****Figures**

**Coordinating Lead Authors:** Gerald A. Meehl (USA), Thomas F. Stocker (Switzerland)

**Lead Authors:** William Collins (USA), Pierre Friedlingstein (France), Amadou Gaye (Senegal), Jonathan Gregory (UK), Akio Kitoh (Japan), Reto Knutti (Switzerland), James Murphy (UK), Akira Noda (Japan), Sarah Raper (UK), Ian Watterson (Australia), Andrew Weaver (Canada), Zong-Ci Zhao (China)

**Contributing Authors:** R. Alley (USA), J. Annan (Japan, UK), J. Arblaster (USA, Australia), C. Bitz (USA), A. le Brocq (UK), P. Brockmann (France), V. Brovkin (Germany, Russia), L. Buja (USA), P. Cadule (France), G. Clarke (Canada), M. Collier (Australia), M. Collins (UK), E. Driesschaert (Belgium), N.A. Diansky (Russia), M. Dix (Australia), K. Dixon (USA), J.-L. Dufresne (France), M. Dyurgerov (USA), M. Eby (Canada), N. Edwards (UK), S. Emori (Japan), P. Forster (UK), R. Furrer (USA, Switzerland), P. Glecker (USA), J. Hansen (USA), G. Harris (UK, New Zealand), G. Hegerl (USA, Germany), M. Holland (USA), A. Hu (USA, China), P. Huybrechts (Belgium), C. Jones (UK), F. Joos (Switzerland), J. Jungclaus (Germany), J. Kettleborough (UK), M. Kimoto (Japan), T. Knutson (USA), M. Krynitzky (USA), D. Lawrence (USA), M.-F. Loutre (Belgium), J. Lowe (UK), D. Matthews (Canada), M. Meinshausen (USA, Germany), S. Müller (Switzerland), S. Nawrath (Germany), J. Oerlemans (The Netherlands), M. Oppenheimer (USA), J. Orr (France), J. Overpeck (USA), T. Palmer (ECMWF), A. Payne (UK), G.-K. Plattner (Switzerland), J. Räisänen (Finland), A. Rinke (Germany), E. Roeckner (Germany), G.L. Russell (USA), D. Salas y Melia (France), B. Santer (USA), G. Schmidt (USA, UK), A. Schmittner (USA, Germany), B. Schneider (Germany), A. Shepherd (UK), A. Sokolov (USA, Russia), D. Stainforth (UK), P. Stott (UK), R. Stouffer (USA), K. Taylor (USA), C. Tebaldi (USA), H. Teng (USA, China), L. Terray (France), D. Vaughan (UK), E. M. Volodin (Russia), B. Wang (China), T. M. L. Wigley (USA), M. Wild (Switzerland), R. van de Wal (The Netherlands), J. Yoshimura (Japan), Y. Yu (China), S. Yukimoto (Japan)

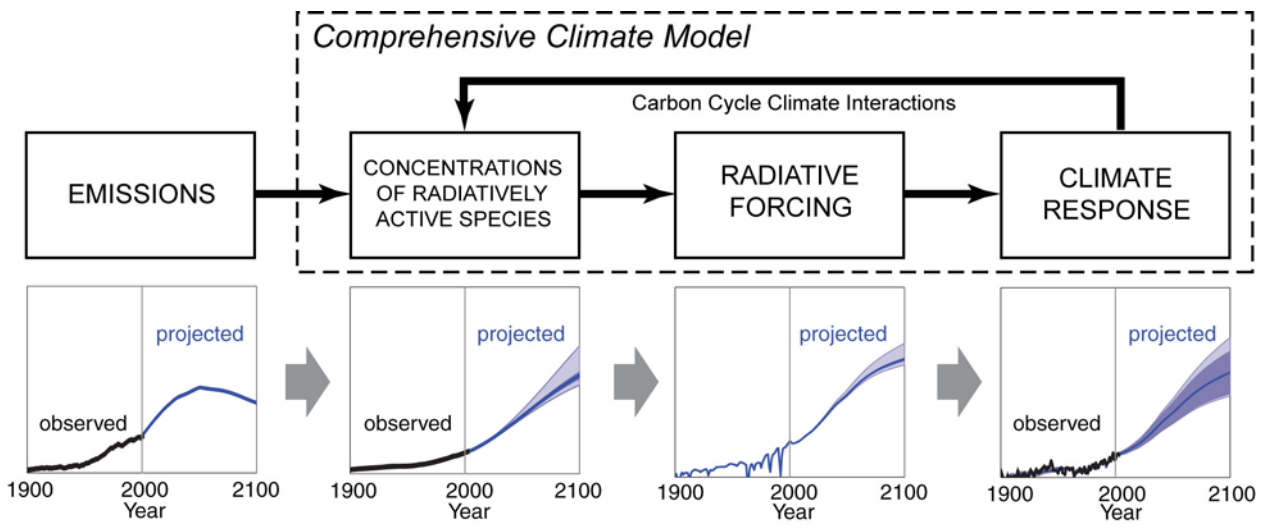
**Review Editors:** Myles Allen (UK), Govind Ballabh Pant (India)

**Date of Draft:** 27 October 2006

---

1

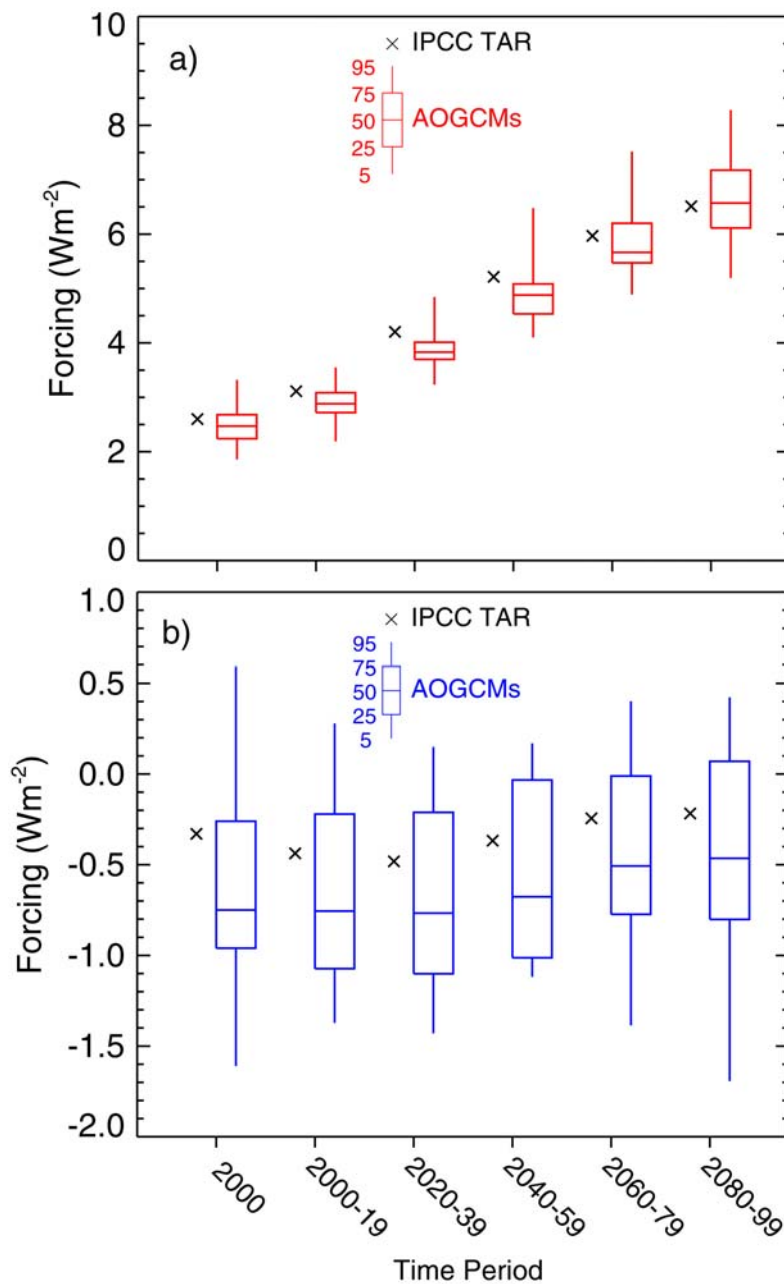
2



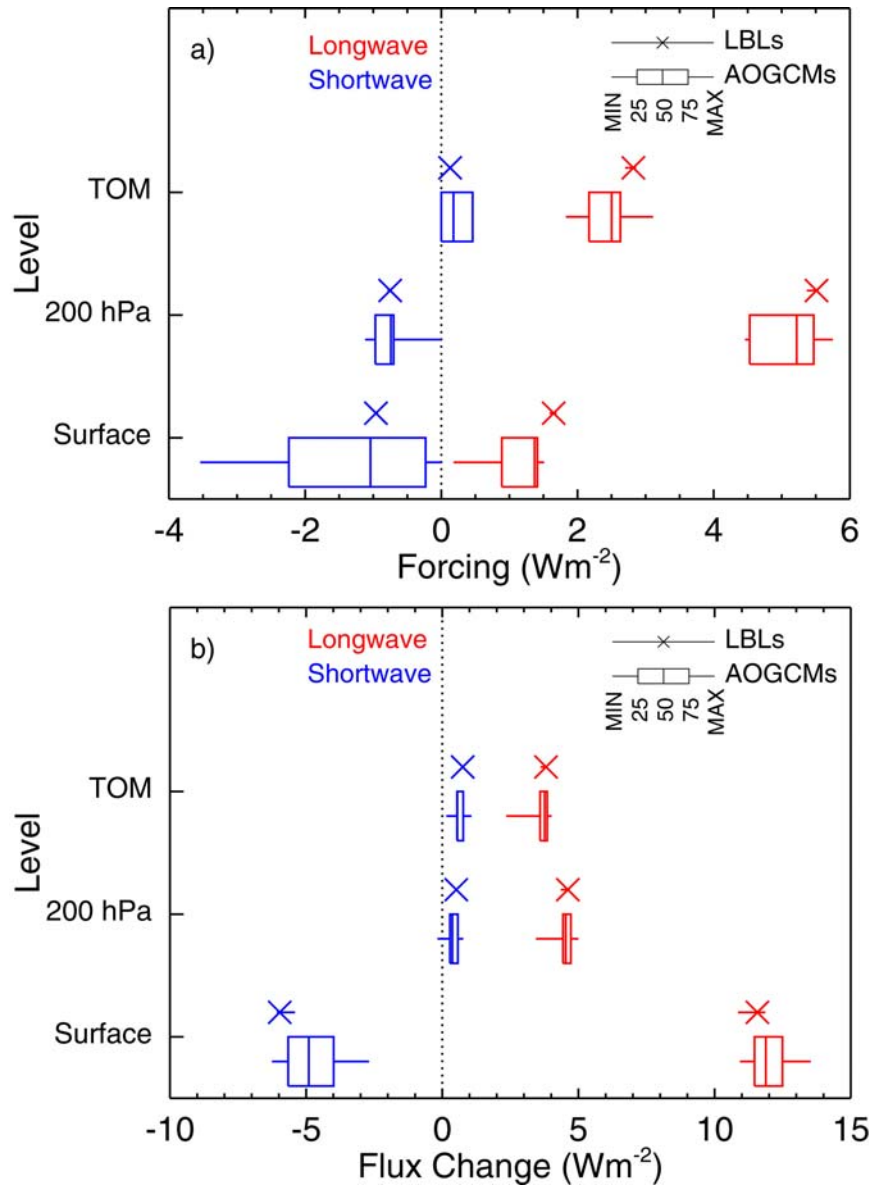
3

4

5 **Figure 10.1.** Several steps from emissions to climate response contribute to the overall uncertainty of a  
 6 climate model projection. These uncertainties can be quantified through a combined effort of observation,  
 7 process understanding, a hierarchy of climate models, and ensemble simulations. In a comprehensive climate  
 8 model, physical and chemical representations of processes permit a consistent quantification of uncertainty.  
 9 Note that the uncertainty associated with the future emission path is of an entirely different nature and not  
 10 part of Chapter 10. Bottom row adapted from Figure 10.25, A1B scenario, for illustration only.  
 11

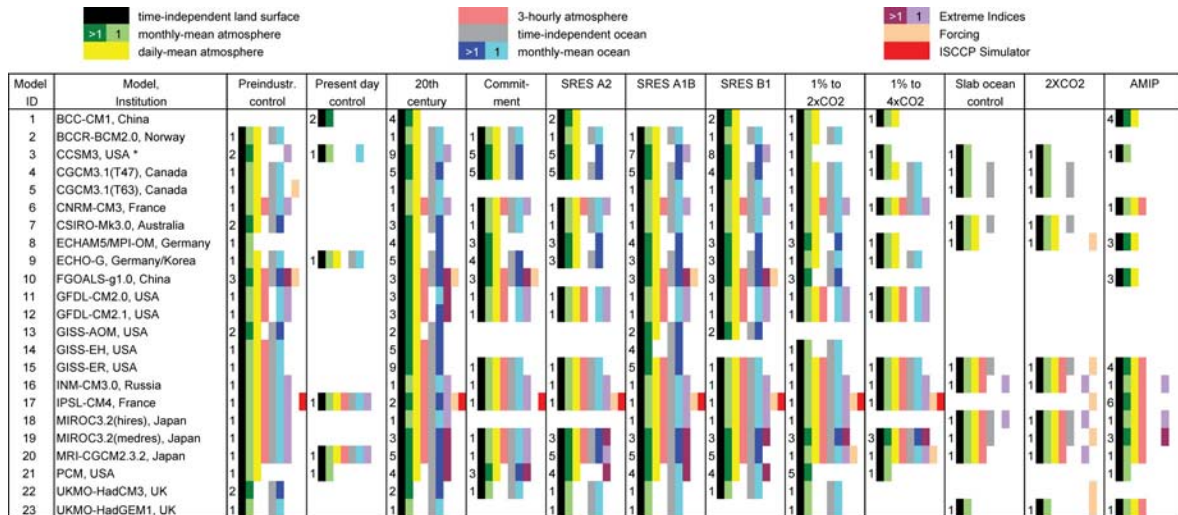
1  
23  
4  
5  
6  
7  
8  
9  
10  
11  
12  
13  
14  
15  
16

**Figure 10.2.** Radiative forcings for the period 2000–2100 for the SRES A1B scenario diagnosed from AOGCMs and from the IPCC TAR (2001) forcing formulas (Forster and Taylor, 2006). a) longwave forcing; b) shortwave forcing. The AOGCM results are plotted with box-and-whisker diagrams representing percentiles of forcings computed from 20 models in the AR4 multi-model ensemble. The central line within each box represents the median value of the model ensemble. The top and bottom of each box shows the 75th and 25th percentiles, and the top and bottom of each whisker displays the 95th and 5th percentile values in the ensemble, respectively. The models included are CCSM3, CGCM3.1(T47 and T63), CNRM-CM3, CSIRO-Mk3, ECHAM5/MPI-OM, ECHO-G, FGOALS-g1.0, GFDL-CM2.0, GFDL-CM2.1, GISS-EH, GISS-ER, INM-CM3.0, IPSL-CM4, MIROC3.2(medium and high resolution), MRI-CGCM2.3.2, PCM1, UKMO-HadCM3, and UKMO-HadGEM1.

1  
23  
4  
5  
6  
7  
8  
9  
10  
11  
12  
13  
14  
15  
16  
17  
18  
19

**Figure 10.3.** Comparison of shortwave and longwave instantaneous radiative forcings and flux changes computed from AOGCMs and line-by-line (LBL) radiative transfer codes (W.D. Collins et al., 2006). a) instantaneous forcing from doubling CO<sub>2</sub> from its concentration in 1860; b) changes in radiative fluxes caused by the 20% increase in H<sub>2</sub>O expected in the climate produced from doubling CO<sub>2</sub>. The forcings and flux changes are computed for clear-sky conditions in mid-latitude summer and do not include effects of stratospheric adjustment. No other well-mixed greenhouse gases are included. The minimum-to-maximum range and median are plotted for five representative LBL codes. The AOGCM results are plotted with box-and-whisker diagrams (see caption for Figure 10.2) representing percentiles of forcings from 20 models in the AR4 multi-model ensemble. The AOGCMs included are BCCR-BCM2.0, CCSM3, CGCM3.1(T47 and T63), CNRM-CM3, ECHAM5/MPI-OM, ECHO-G, FGOALS-g1.0, GFDL-CM2.0, GFDL-CM2.1, GISS-EH, GISS-ER, INM-CM3.0, IPSL-CM4, MIROC3.2 (medium and high resolution), MRI-CGCM2.3.2, PCM, UKMO-HadCM3, and UKMO-HadGEM1. The LBL codes are the GFDL LBL, GISS LBL3, NCAR/ICSTM GENLN2, NASA LaRC MRTA, and the University of Reading RFM.

1  
2

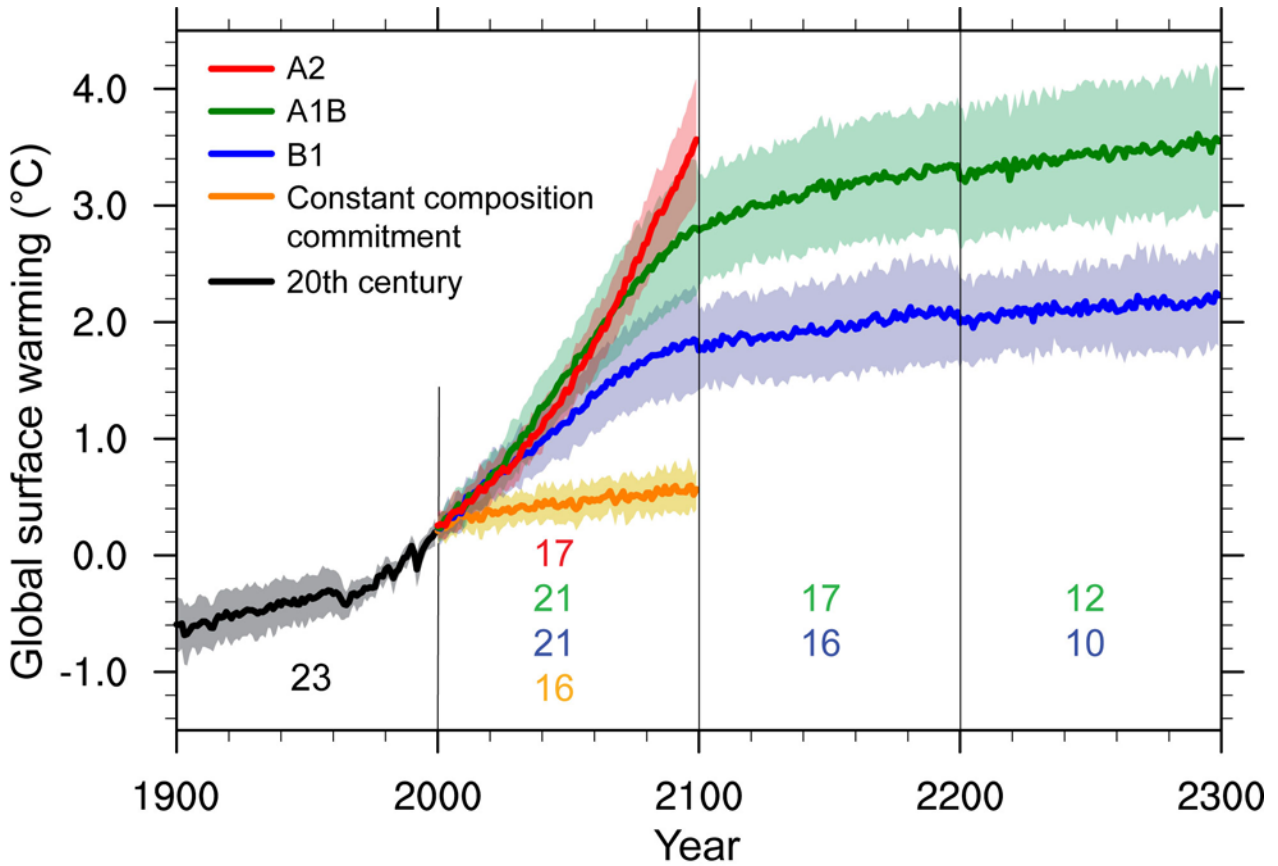


3  
4  
5  
6  
7  
8  
9  
10  
11  
12  
13  
14  
15  
16

**Table 10.4.** Summary of climate change model experiments produced with AOGCMs. Numbers in each scenario column indicate how many ensemble members were produced for each model. Coloured fields indicate that some but not necessarily all variables of the specific data type (separated by climate system component and time interval) were available for download at PCMDI to be used in this report. Additional data has been submitted for some models and may subsequently become available. Where different color shadings are given in the legend, the colour indicates whether data from a single or from multiple ensemble members is available. Details on the scenarios, variables and models can be found at the PCMDI webpage ([http://www-pcmdi.llnl.gov/ipcc/about\\_ipcc.php](http://www-pcmdi.llnl.gov/ipcc/about_ipcc.php)). Status: August 2006. Model IDs are the same as in Chapter 8, Table 8.8.1.

\* Some of the ensemble members using the CCSM3 were run on the Earth Simulator in Japan in collaboration with CRIEPI.

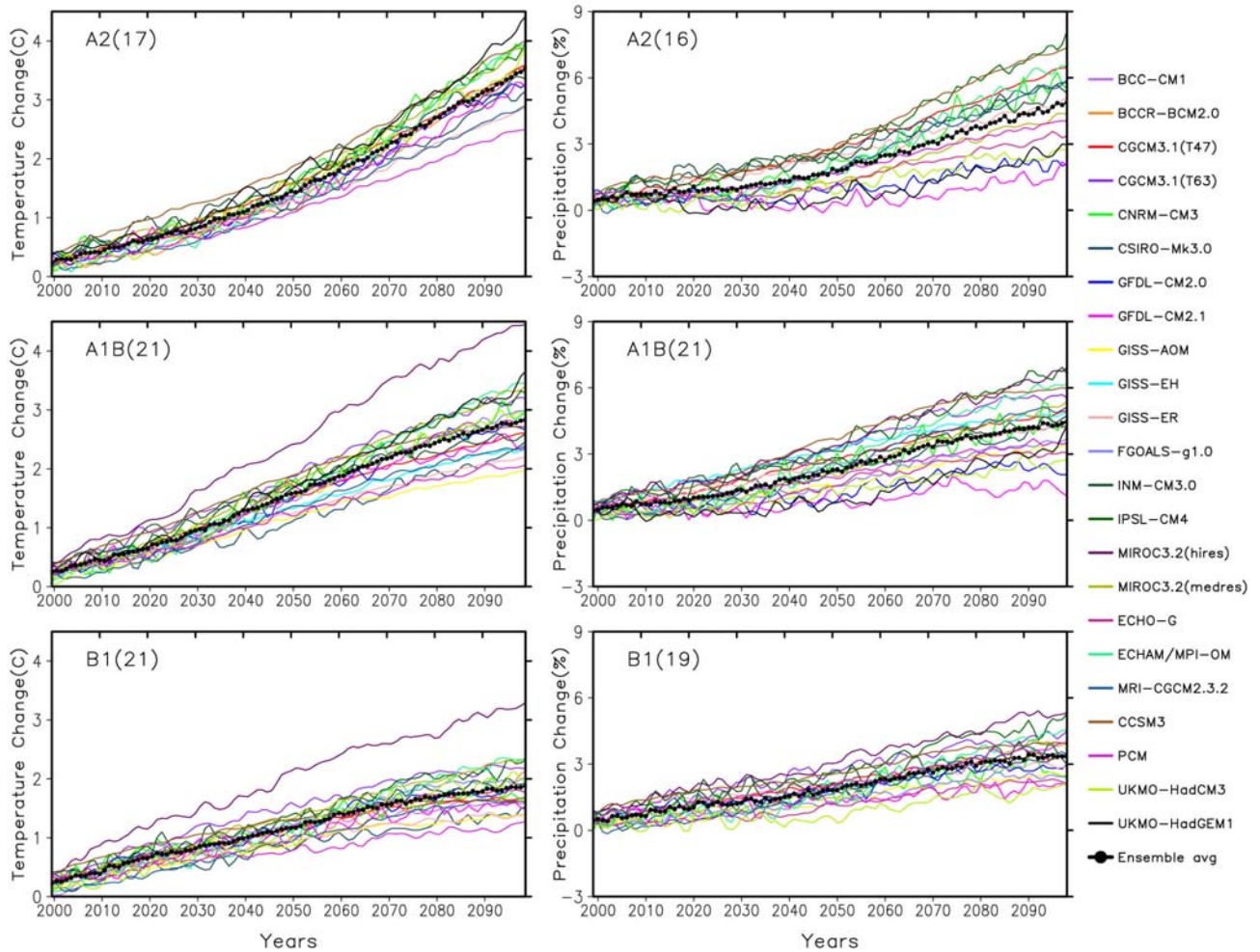
1  
2



3  
4  
5  
6  
7  
8  
9  
10  
11  
12  
13  
14

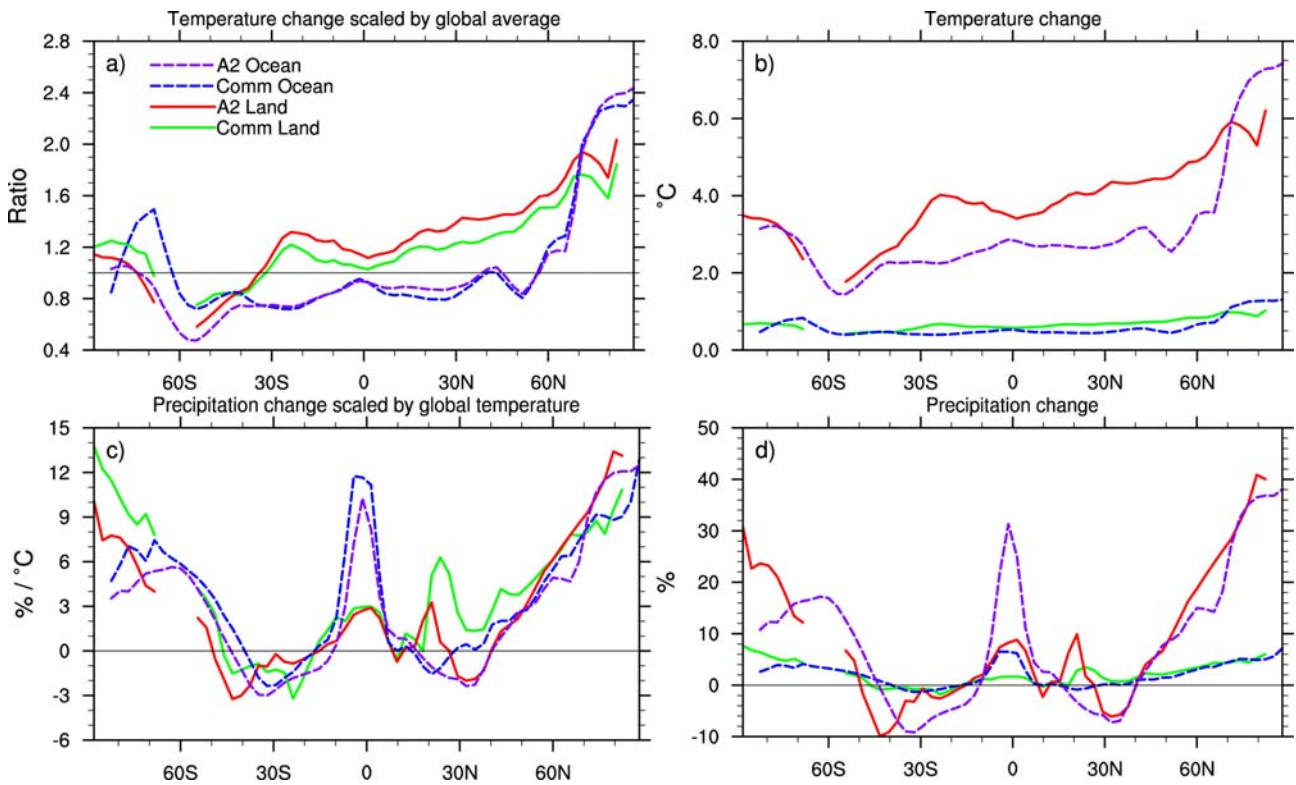
**Figure 10.4.** Multi-model means of surface warming (relative to 1980–1999) for the scenarios A2, A1B and B1, shown as continuations of the 20th century simulation. Values beyond 2100 are for the stabilization scenarios (see Section 10.7). Linear trends from the corresponding control runs have been removed from these time series. Lines show the multi model means, shading denotes the plus minus one standard deviation range of individual model annual means. Discontinuities between different periods have no physical meaning and are caused by the fact that the number of models that have run a given scenario is different for each period and scenario, as indicated by the coloured numbers given for each phase and scenario at the bottom of the panel. For the same reason, uncertainty across scenarios should not be interpreted from this figure (see Section 10.5.4.6 for uncertainty estimates).

1  
2

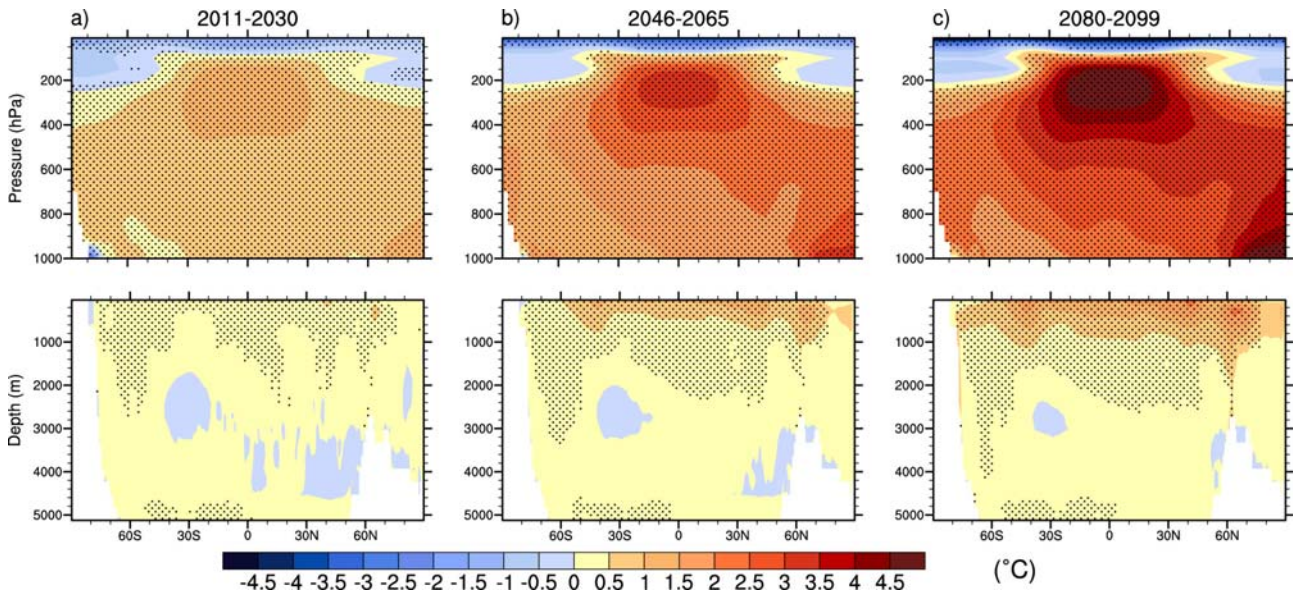


3  
4  
5  
6  
7  
8  
9  
10  
11

**Figure 10.5.** Time series of globally averaged (left) surface warming (surface air temperature change, in °C) and (right) precipitation change (in %) from the various global coupled models for the scenarios A2 (top), A1B (middle) and B1 (bottom). Values are annual means, relative to the 1980–1999 average from the corresponding 20th century simulations, with any linear trends in the corresponding control run simulations removed. A 3-point smoothing was applied. Multi-model (ensemble) mean series are marked with black dots.

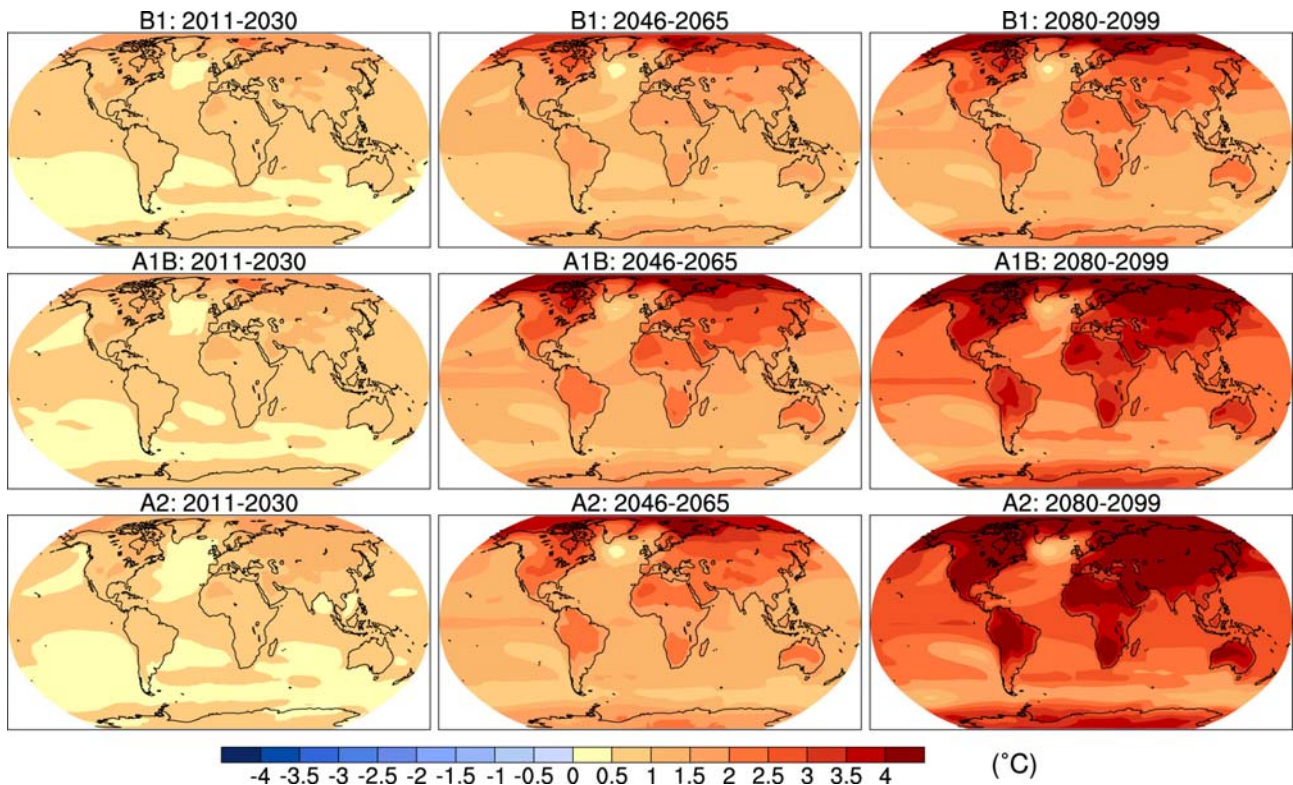
1  
23  
4  
5  
6  
7  
8  
9  
10

**Figure 10.6.** Zonal means taken over land and ocean separately, for annual mean surface warming (panels a and b) and precipitation (panels c and d), shown as a ratios scaled (a, c) and not scaled (b, d) with the global mean warming. Multi-model mean results are shown for two scenarios, A2 and Commitment (see Section 10.7), for the period 2080–2099 relative to the zonal means for 1980–1999. Results for individual models can be seen in supplementary material for this chapter.

1  
23  
4  
5  
6  
7  
8  
9  
10

**Figure 10.7.** Zonal means of change in atmospheric and oceanic temperatures, shown as cross sections. Values are the multi-model means for the A1B scenario for three periods (a-c). Stippling denotes regions where the multi-model ensemble mean divided by the multi-model standard deviation exceeds 1.0 (in magnitude). Anomalies are given relative to the average of the period 1980–1999. Results for individual models can be seen in supplementary material for this chapter.

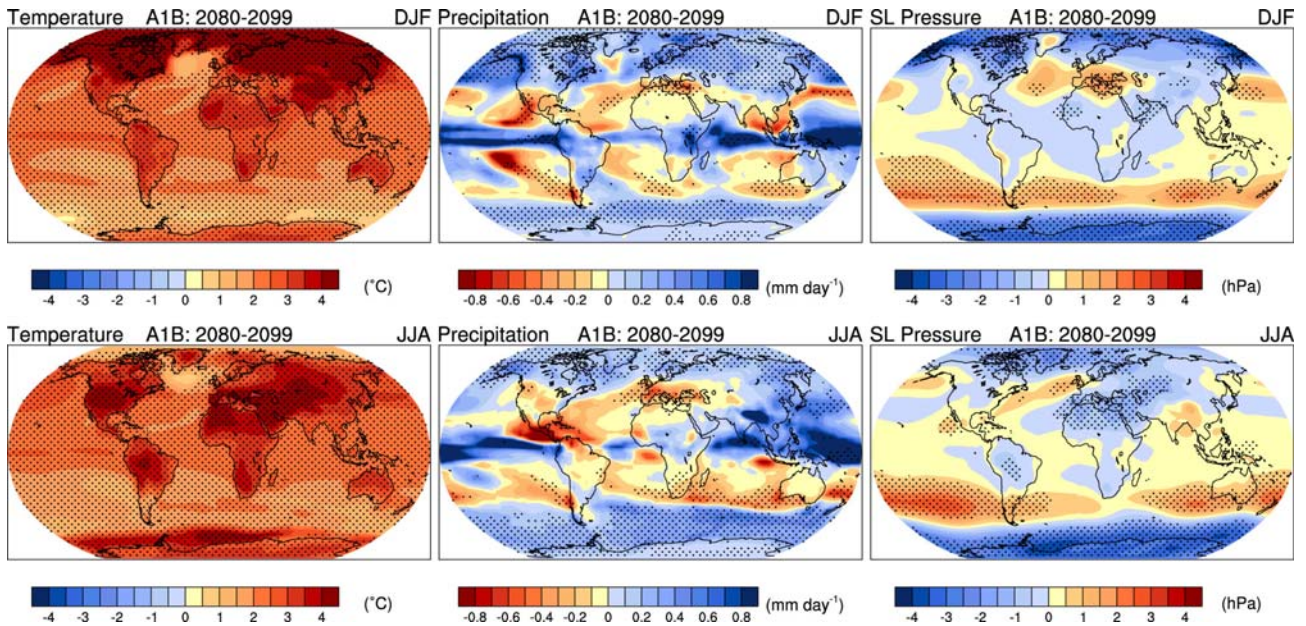
1  
2



3  
4  
5  
6  
7  
8  
9  
10

**Figure 10.8.** Multi-model mean of annual mean surface warming (surface air temperature change, in °C) for the scenarios B1 (top), A1B (middle) and A2 (bottom), and three time periods, 2011–2030 (left), 2046–2065 (middle), and 2080–2099 (right). Stippling is omitted for clarity (see text). Anomalies are given relative to the average of the period 1980–1999. Results for individual models can be seen in supplementary material for this chapter.

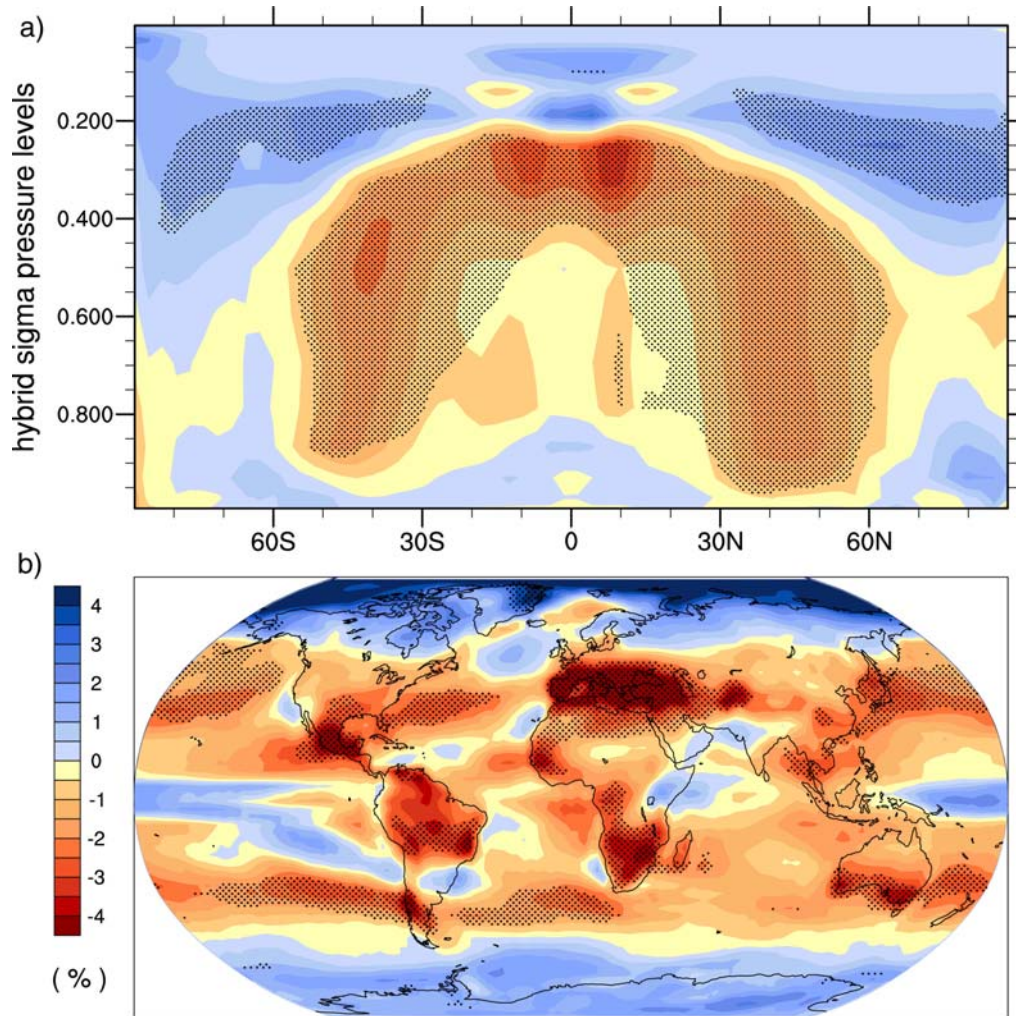
1  
2



3  
4  
5  
6  
7  
8  
9  
10

**Figure 10.9.** Multi-model mean changes of surface air temperature ( $^{\circ}\text{C}$ , left), precipitation ( $\text{mm day}^{-1}$ , middle), and sea level pressure (hPa, right) for boreal winter (DJF, top) and summer (JJA, bottom). Changes are given for the scenarios SRES A1B, for the period 2080–2099 relative to 1980–1999. Stippling denotes areas where the magnitude of the multi-model ensemble mean exceeds the inter-model standard deviation. Results for individual models can be seen in supplementary material for this chapter.

1



2

3

4

5

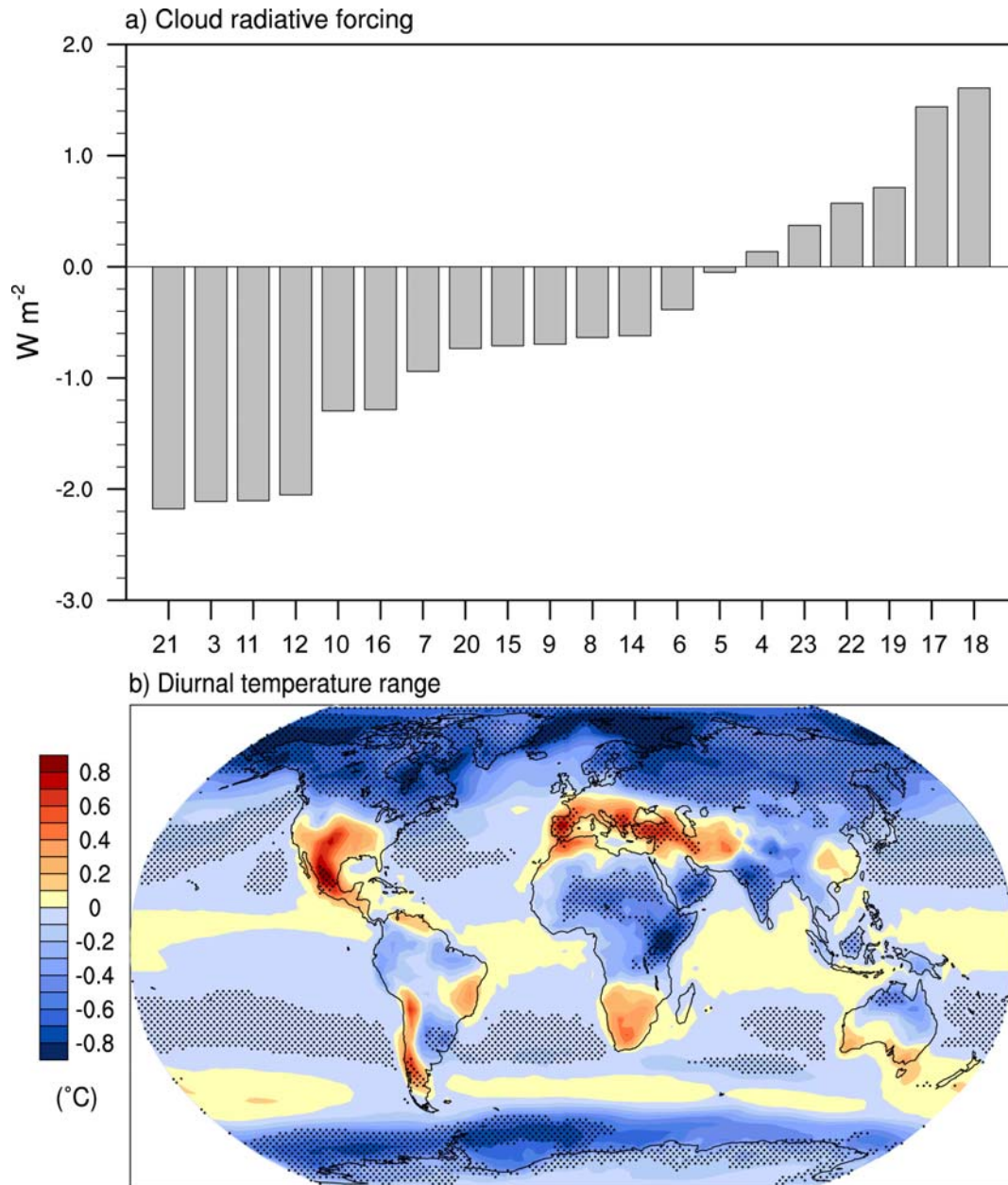
6

7

8

9

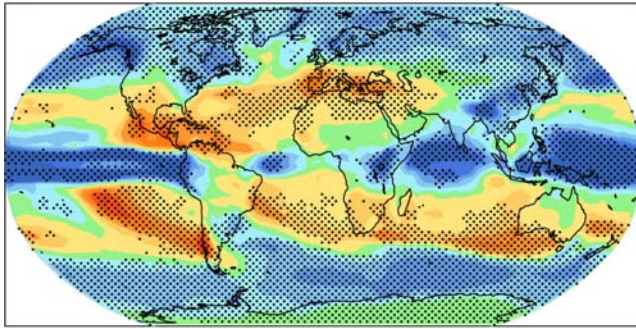
**Figure 10.10.** Multi model mean changes in a) zonal mean cloud fraction (in %), shown as a cross section through the atmosphere, and b) total cloud area fraction (in percentage cover from all models). Changes are given as annual means for the scenarios SRES A1B, for the period 2080–2099 relative to 1980–1999. Stippling denotes areas where the magnitude of the multi-model ensemble mean exceeds the inter-model standard deviation. Results for individual models can be seen in supplementary material for this chapter.

1  
23  
4  
5  
6  
7  
8  
9  
10

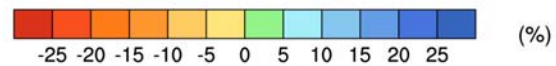
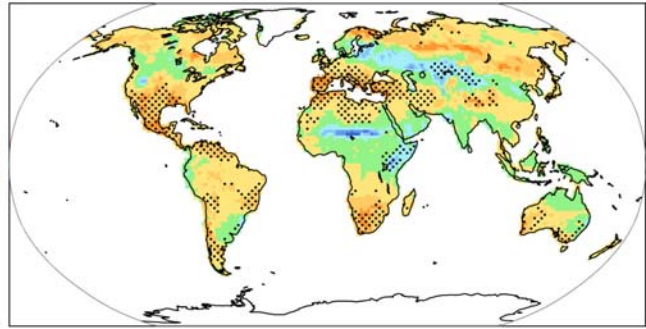
**Figure 10.11.** Changes in a) global mean cloud radiative forcing (in  $\text{W m}^{-2}$ ) from individual models (see Table 10.4 for the list of models), and b) multi-model mean diurnal temperature range ( $^{\circ}\text{C}$ ). Changes are annual means for the scenarios SRES A1B, for the period 2080–2099 relative to 1980–1999. Stippling denotes areas where the magnitude of the multi-model ensemble mean exceeds the inter-model standard deviation. Results for individual models can be seen in supplementary material for this chapter.

1  
2

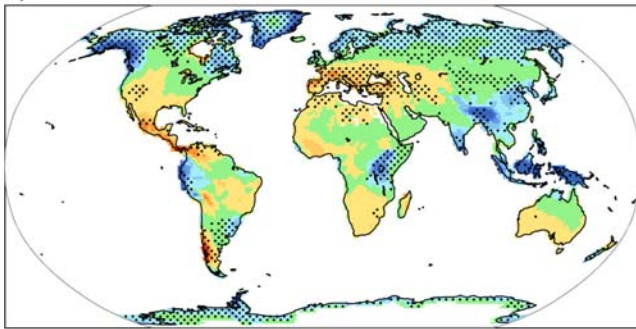
a) Precipitation



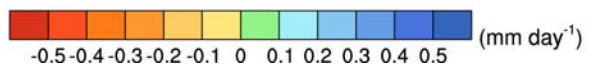
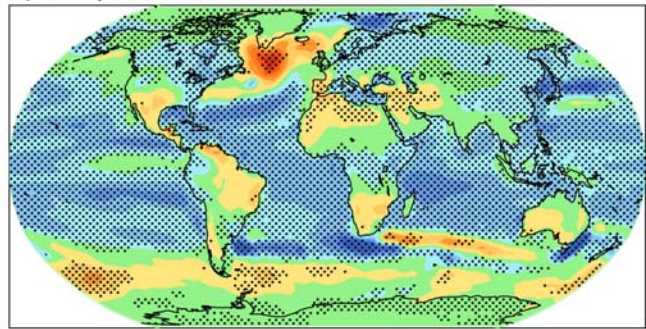
b) Soil moisture



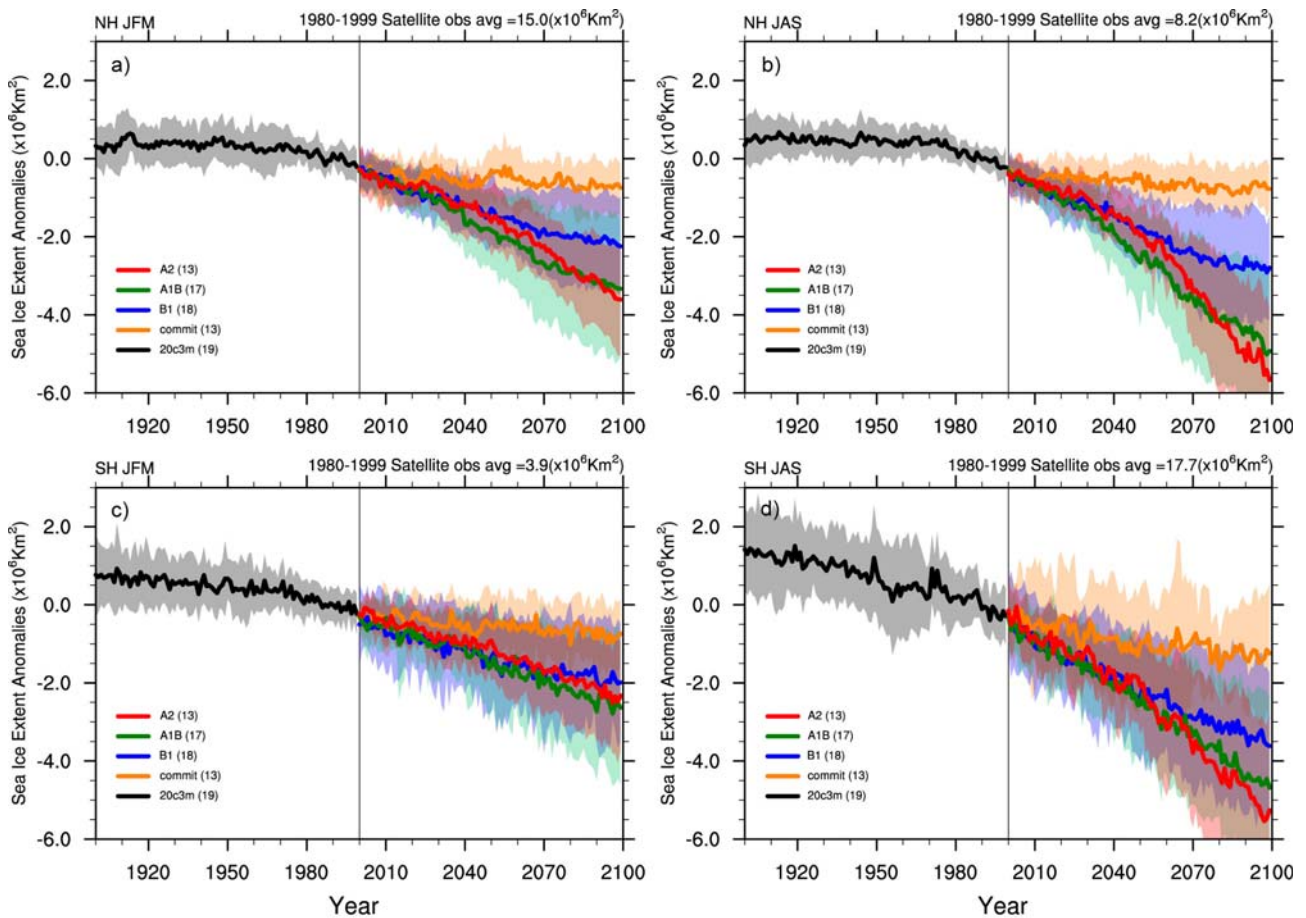
c) Runoff



d) Evaporation

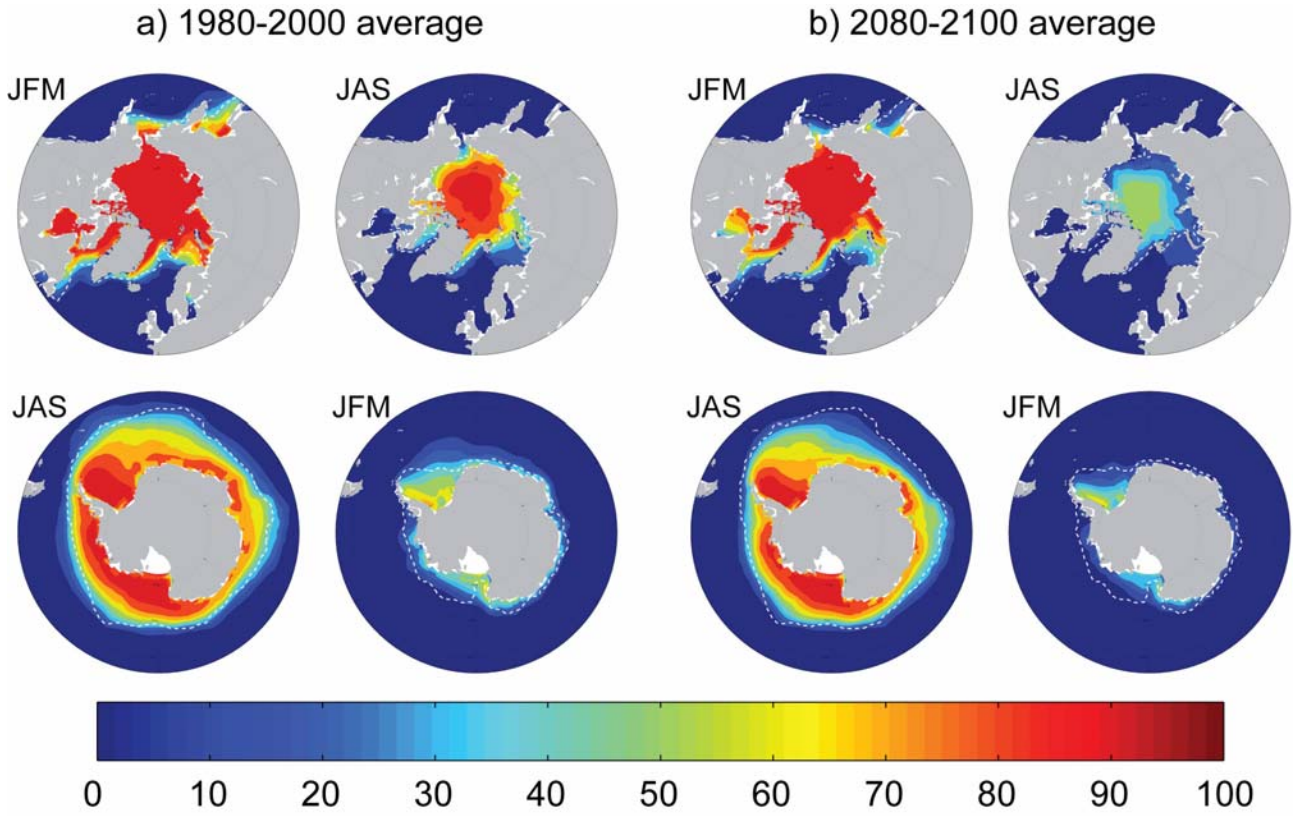
3  
4  
5  
6  
7  
8  
9  
10  
11  
12

**Figure 10.12.** Multi-model mean changes in a) precipitation ( $\text{mm day}^{-1}$ ), b) soil moisture content (%), c) runoff ( $\text{mm day}^{-1}$ ), and d) evaporation ( $\text{mm day}^{-1}$ ). To indicate consistency of sign of change, regions are stippled where at least 80% of models agree on the sign of the mean change. Changes are annual means for the scenarios SRES A1B, for the period 2080–2099 relative to 1980–1999. Soil moisture and runoff changes are shown at land points with valid data from at least 10 models. Details of the method and results for individual models can be found in supplementary material for this chapter (Appendix S10.1).

1  
2

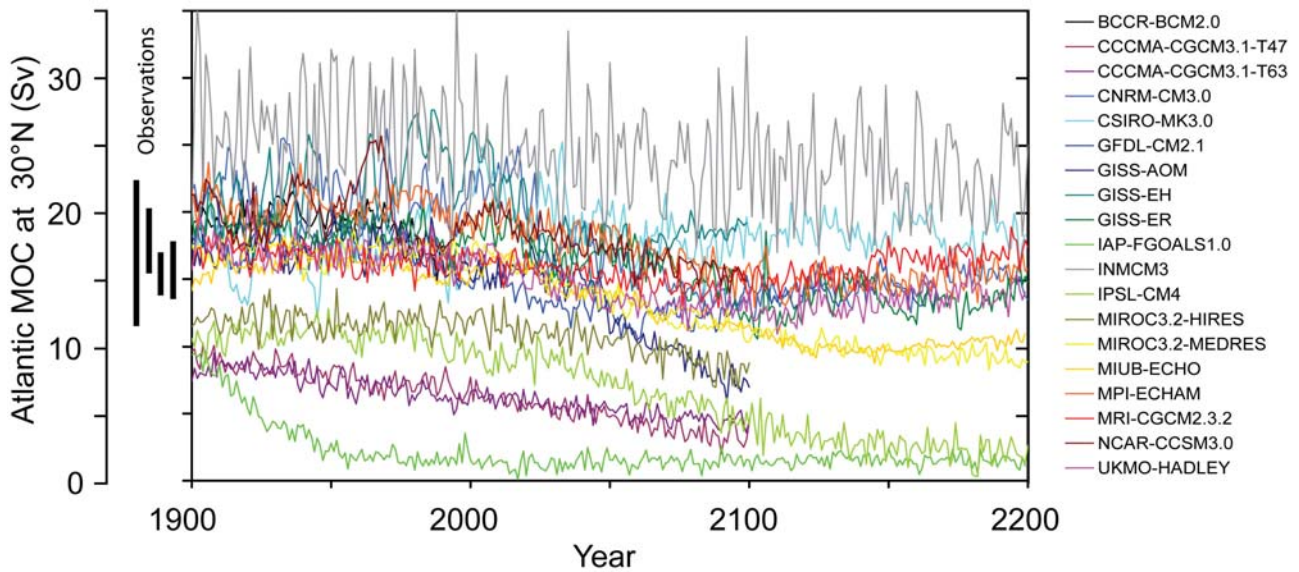
3  
4 **Figure 10.13.** Multi model simulated anomalies in sea ice extent for the 20th century, the SRES A2, A1B  
5 and B1 as well as the commitment scenario, for a) Northern Hemisphere January to March (JFM), b)  
6 Northern Hemisphere July to September (JAS). Panels c and d are as for a and b but for the Southern  
7 Hemisphere. The solid lines show the multi model mean, shaded areas denote plus minus one standard  
8 deviation. Sea ice extent is defined as the total area where sea ice concentration exceeds 15%. Anomalies are  
9 shown relative to the period 1980–2000. The number of models is given in the legend and is different for  
10 each scenario.  
11

1  
2



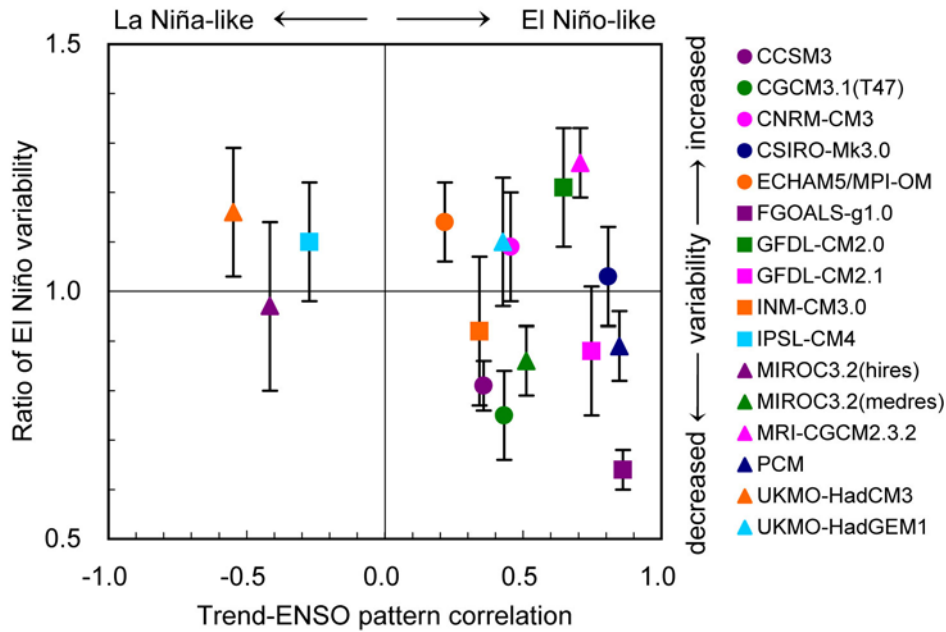
3  
4  
5  
6  
7  
8  
9  
10

**Figure 10.14.** Multi-model mean sea ice concentration (in %) for January to March (JFM) and June to September (JAS), Arctic (top) and Antarctic (bottom) for the periods a) 1980–2000 and b) 2080–2100 for the scenario SRES A1B. The dashed white line indicates the present-day 15% average sea-ice concentration limit. Modified from Flato et al. (2004).

1  
23  
4  
5  
6  
7  
8  
9  
10  
11  
12  
13  
14  
15  
16  
17

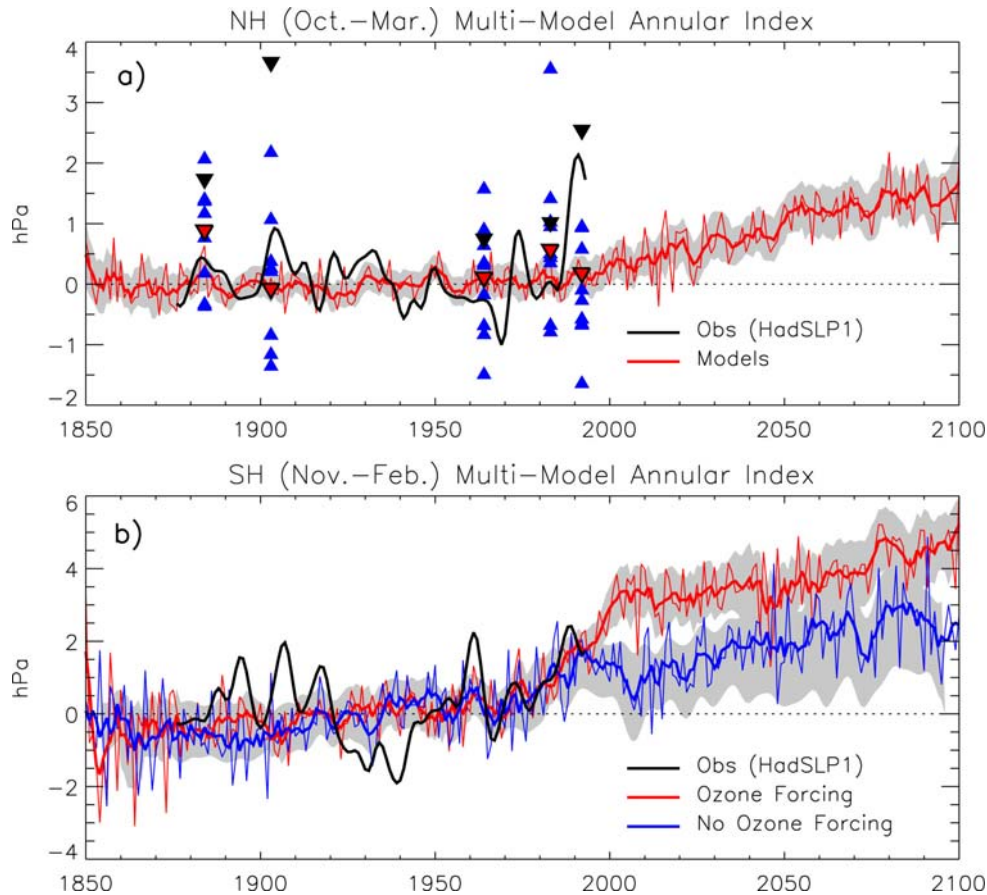
**Figure 10.15.** Evolution of the Atlantic meridional overturning circulation (MOC) at 30°N in simulations with the suite of comprehensive coupled climate models from 1850 to 2100 using scenarios 20C3M for 1850 to 1999 and emissions scenario SRES A1B for 1999 to 2100. Some of the models continue the integration to year 2200 with the forcing held constant at the values of year 2100. Observationally based estimates of late 20th century MOC are given as vertical bars on the left. Three simulations show a steady or rapid spin down of the MOC which is unrelated to the forcing; a few others have late 20th century simulated values that are inconsistent with observational estimates. Of the model simulations consistent with the late 20th century observational estimates, no simulation shows an increase of MOC during the 21st century; reductions range from indistinguishable within the simulated natural variability to over 50% relative to the 1960–1990 mean; none of the models projects an abrupt transition to an off state of the MOC. Adapted from Schmittner et al., (2005) with additions.

1  
2



3  
4  
5  
6  
7  
8  
9  
10  
11  
12  
13  
14  
15  
16  
17  
18  
19

**Figure 10.16** Base state change in average tropical Pacific sea surface temperatures and change in El Niño variability from AOGCMs. The base state change is denoted by the spatial anomaly pattern correlation coefficient between the linear trend of sea surface temperature (SST) in the 1% CO<sub>2</sub> increase climate change experiment and the first EOF of SST in the control experiment over the area 10°S–10°N, 120°E–80°W (reproduced from Yamaguchi and Noda (2006)). Positive correlation values indicate that the mean climate change has an El Niño-like pattern, and negative values are La Niña-like. The change in El Niño variability is denoted by the ratio of the standard deviation of the first EOF of sea level pressure (SLP) between the current climate and the last 50 years of the SRES A2 experiments (2051–2100), except for FGOALS-g1.0 and MIROC3.2(hires) for which the SRES A1B was used, and UKMO-HadGEM1 for which the 1% CO<sub>2</sub> increase climate change experiment was used, in the region 30°S–30°N, 30°E–60°W with a 5-month running mean (reproduced from van Oldenborgh et al. (2005)). Error bars indicate the 95% confidence interval. Note that tropical Pacific base state climate changes with either El Niño-like or La Niña-like patterns are not permanent El Niño or La Niña events, and all still have ENSO interannual variability superimposed on that new average climate state in a future warmer climate.

1  
2

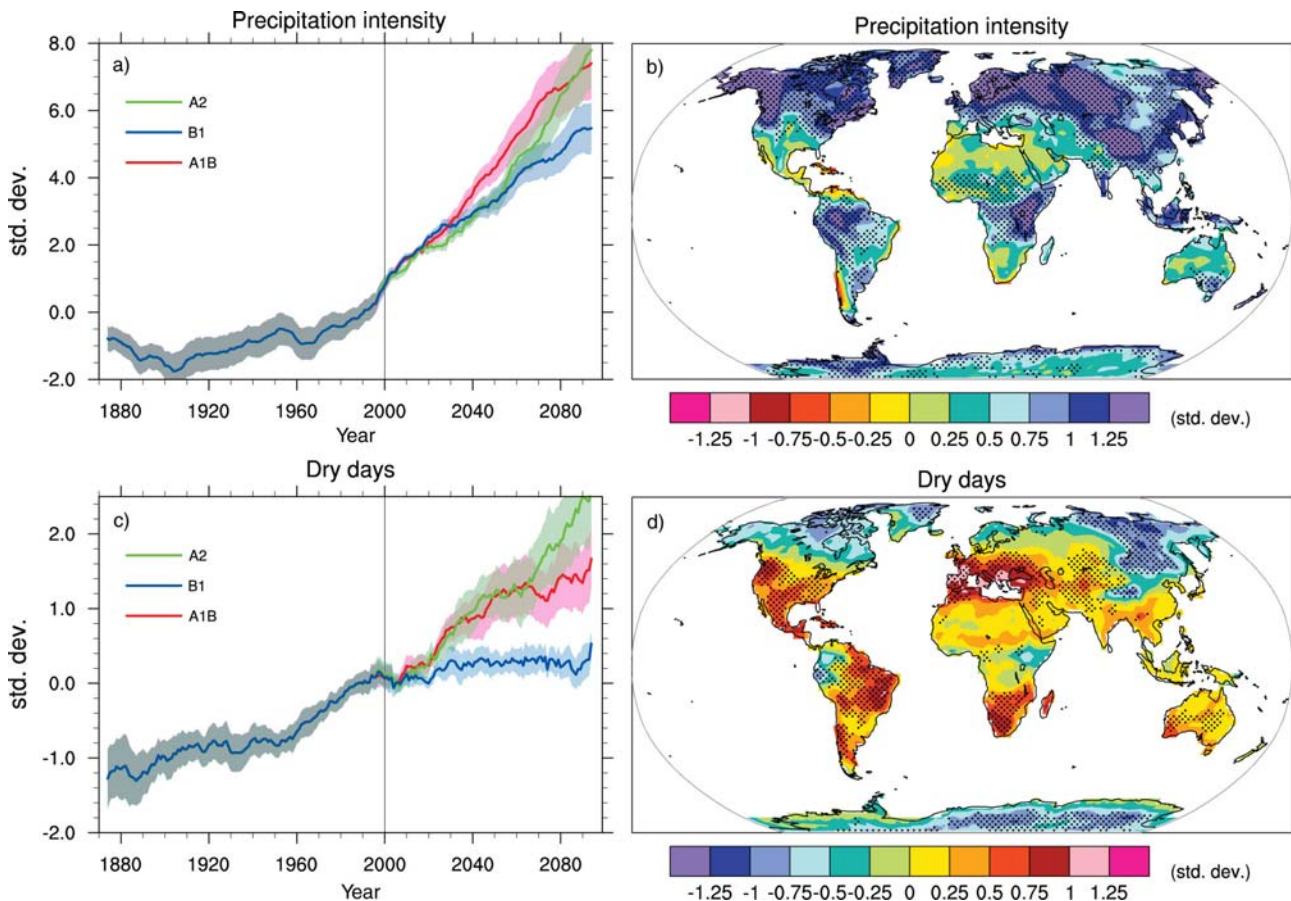
3

4

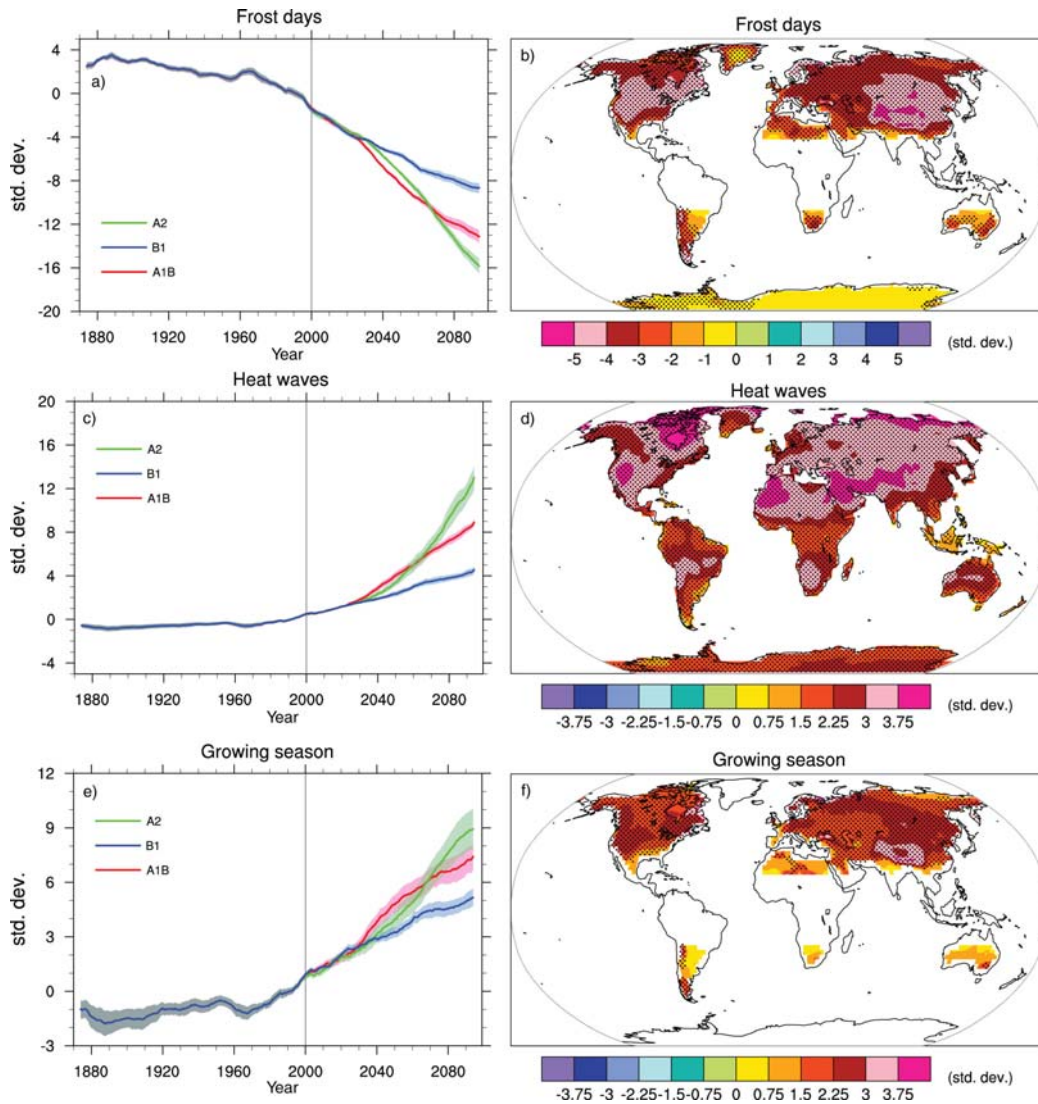
5

6 **Figure 10.17.** (a) Multi model mean of the regression of the leading EOF of ensemble mean Northern  
 7 Hemisphere sea level pressure (NH SLP, thin red). The time series of regression coefficients has zero mean  
 8 between year 1900 and 1970. The thick red line is a 10-year low-pass filtered version of the mean. The  
 9 gray shading represents the inter-model spread at the 95% level and is filtered. A filtered version of the  
 10 observed SLP is in black. The regression coefficient for the winter following a major tropical eruption is  
 11 marked by red, blue, and black triangles, respectively, for the multi-model mean, the individual model mean,  
 12 and observations. (b) as in (a) except for the Southern Hemisphere SLP for models with (red) and without  
 13 (blue) ozone forcing. Adapted from Miller et al. (2006).

14

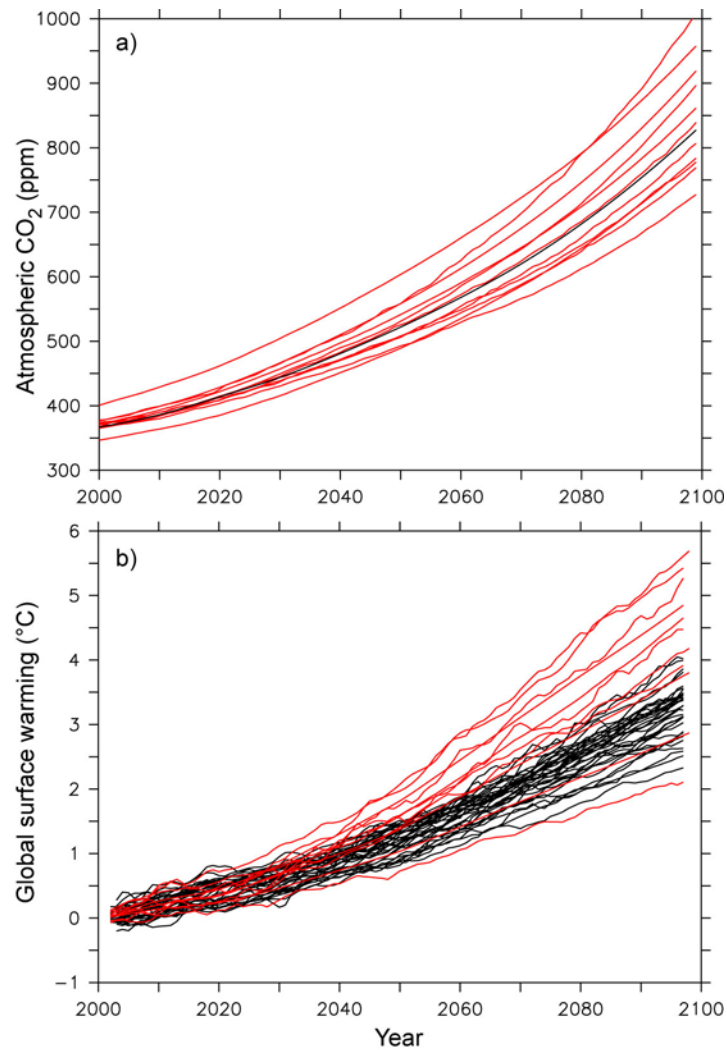
1  
23  
4

5 **Figure 10.18.** Changes in extremes based on multi-model simulations from nine global coupled climate  
6 models, adapted from Tebaldi et al. (2006). a) Globally averaged changes in precipitation intensity (defined  
7 as the annual total precipitation divided by the number of wet days) for a low (SRES B1), middle (SRES  
8 A1B), and high (SRES A2) scenario. b) Changes of spatial patterns of precipitation intensity based on  
9 simulations between two 20-year means (2080–2099 minus 1980–1999) for the A1B scenario. c) Globally  
10 averaged changes in dry days (defined as the annual maximum number of consecutive dry days). d) changes  
11 of spatial patterns of dry days based on simulations between two 20-year means (2080–2099 minus 1980–  
12 1999) for the A1B scenario. Solid lines in panels a and c are the 10-year smoothed multi-model ensemble  
13 means, the envelope indicates the ensemble mean standard deviation. Stippling in panels b and d denote  
14 areas where at least 5 of the 9 models concur in determining that the change is statistically significant.  
15 Extreme indices are calculated only over land. Extremes indices are calculated following Frich et al. (2002).  
16 Each model's timeseries has been centered around its 1980–1999 average and normalized (rescaled) by its  
17 standard deviation computed (after detrending) over the period 1960–2099, then the models were aggregated  
18 into an ensemble average, both at the global average and at the grid-box level. Thus, changes are given in  
19 units of standard deviations.  
20

1  
23  
4

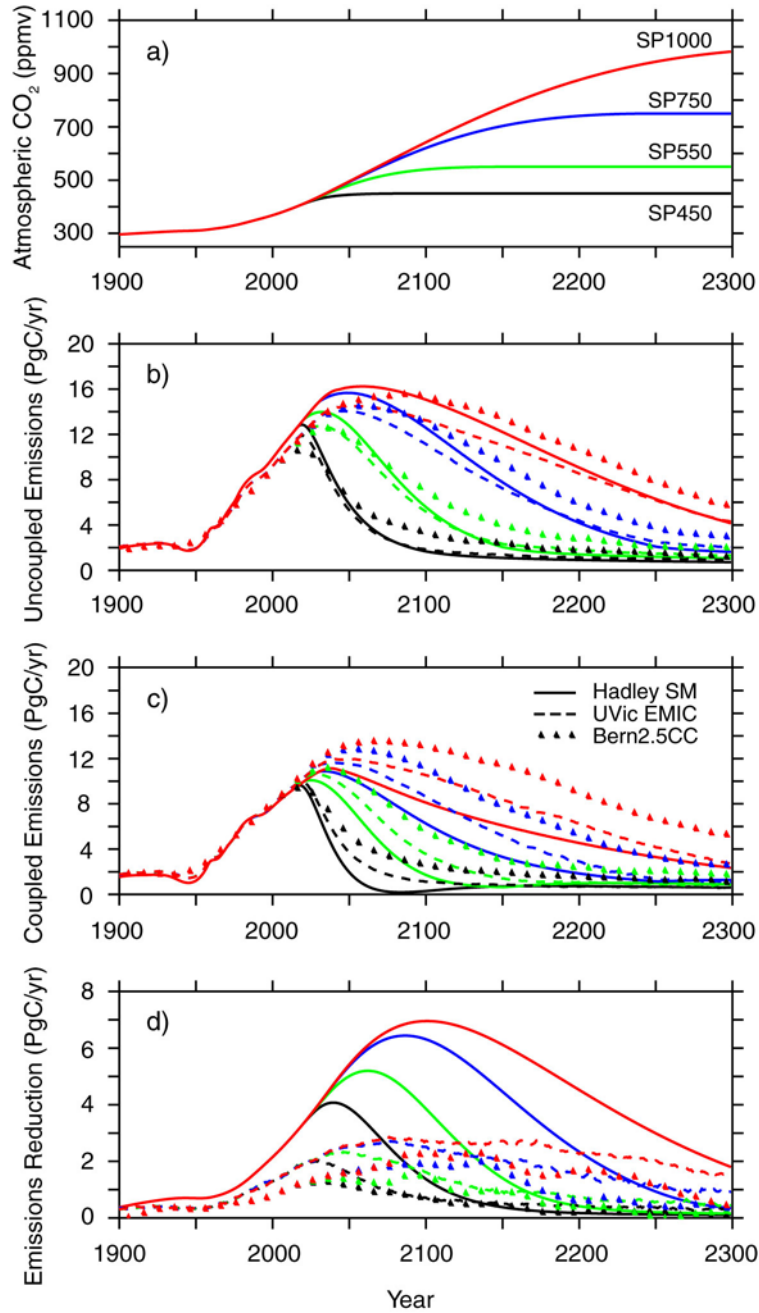
**Figure 10.19.** Changes in extremes based on multi-model simulations from nine global coupled climate models, adapted from Tebaldi et al. (2006). a) Globally averaged changes in frost days (the frost day index is defined as the total number of days in a year with absolute minimum temperature below  $0^{\circ}\text{C}$ ) for a low (SRES B1), middle (SRES A1B), and high (SRES A2) scenario. b) changes of spatial patterns of frost days based on simulations between two 20-year means (2080–2099 minus 1980–1999) for the A1B scenario. c) Globally averaged changes in heat waves (a heat wave is defined as the longest period in the year of at least 5 consecutive days with maximum temperature at least  $5^{\circ}\text{C}$  higher than climatology of the same calendar day). d) changes of spatial patterns of heat waves based on simulations between two 20-year means (2080–2099 minus 1980–1999) for the A1B scenario. e) Globally averaged changes growing season length (the growing season is defined as the length of the period between the first spell of five consecutive days with mean temperature above  $5^{\circ}\text{C}$  and the last such spell of the year). f) changes of spatial patterns of growing season length based on simulations between two 20-year means (2080–2099 minus 1980–1999) for the A1B scenario. Solid lines in panels a, c and e are the 10-year smoothed multi-model ensemble means, the envelope indicates the ensemble mean standard deviation. Stippling in panels b, d and f denote areas where at least 5 of the 9 models concur in determining that the change is statistically significant. Extreme indices are calculated only over land. Frost days and growing season are only calculated in the extratropics. Extremes indices are calculated following Frich et al. (2002). Each model's timeseries has been centered around its 1980–1999 average and normalized (rescaled) by its standard deviation computed (after detrending) over the period 1960–2099, then the models were aggregated into an ensemble average, both at the global average and at the grid-box level. Thus, changes are given in units of standard deviations.

25

1  
23  
4  
5  
6  
7  
8  
9  
10  
11  
12  
13  
14

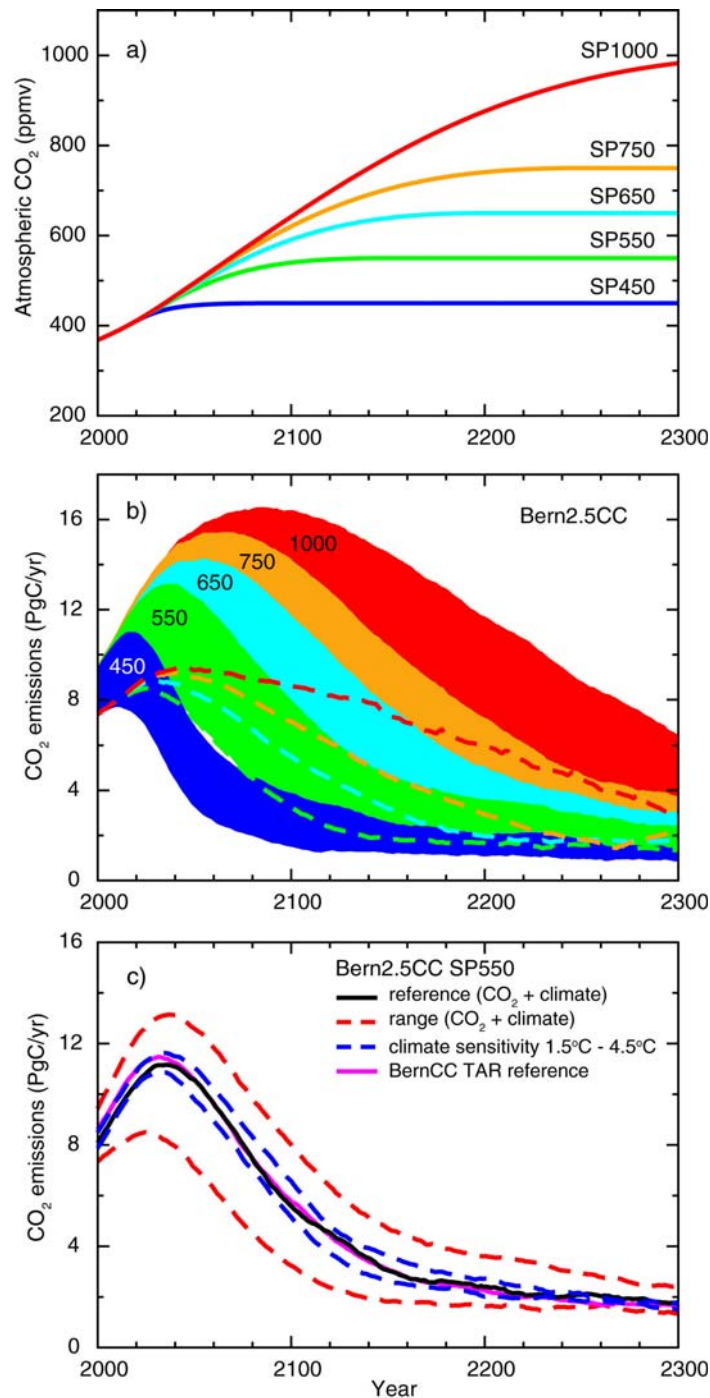
**Figure 10.20.** a) 21st century atmospheric CO<sub>2</sub> concentration as simulated by the 11 C4MIP models for the SRES A2 emission scenario (red) compared with the standard atmospheric CO<sub>2</sub> concentration used as a forcing for many IPCC-AR4 climate models (black). The standard CO<sub>2</sub> concentration values were calculated by the BERN-CC model and are identical to the TAR. For some IPCC-AR4 models, different carbon cycle models were used to convert carbon emissions to atmospheric concentrations; b) Global averaged surface temperature change (relative to 2000) simulated by the C4MIP models forced by CO<sub>2</sub> emissions (red) compared to global warming simulated by the IPCC-AR4 models forced by CO<sub>2</sub> concentration (black). The C4MIP global temperature change has been corrected to account for the non-CO<sub>2</sub> radiative forcing used by the standard IPCC-AR4 climate models.

1  
2

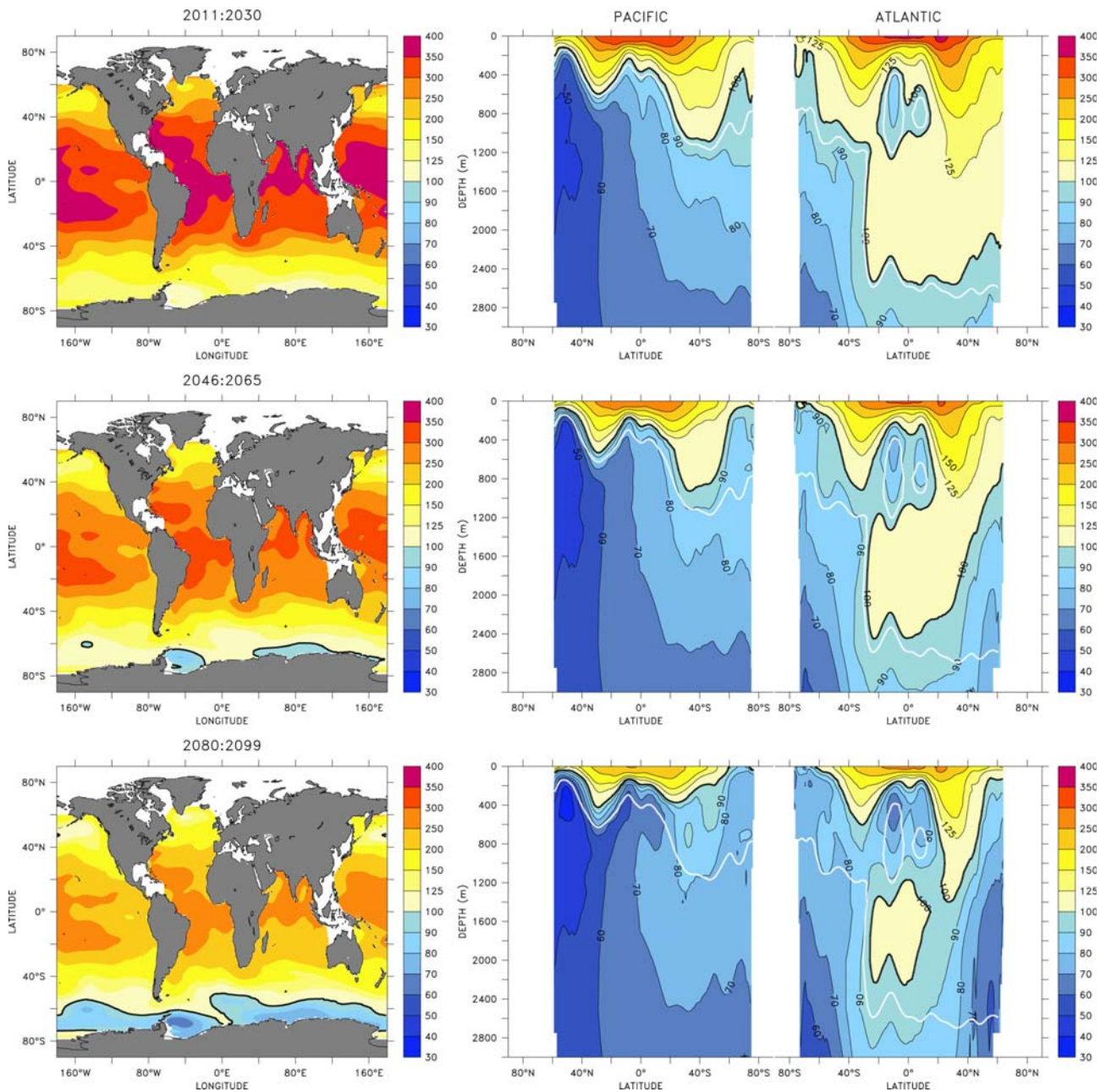


3  
4  
5  
6  
7  
8  
9  
10  
11  
12

**Figure 10.21.** a) Atmospheric CO<sub>2</sub> stabilization scenarios, SP1000 (red), SP750 (blue), SP550 (green) and SP450 (black). b) Compatible annual emissions calculated by three models, Hadley simple model (Jones et al., 2006) (solid), UVic EMIC (Matthews, 2005)(dashed) and BERN2.5CC EMIC (Joos et al., 2001; Plattner et al., 2001) (triangles) for the three stabilization scenarios without accounting for the impact of climate on the carbon cycle. c) Same as b) but when the climate impact on the carbon cycle is accounted for. d) Difference between b) and c) showing the impact of the climate-carbon cycle feedback on the calculation of compatible emissions.

1  
23  
4  
5  
6  
7  
8  
9  
10  
11  
12  
13  
14

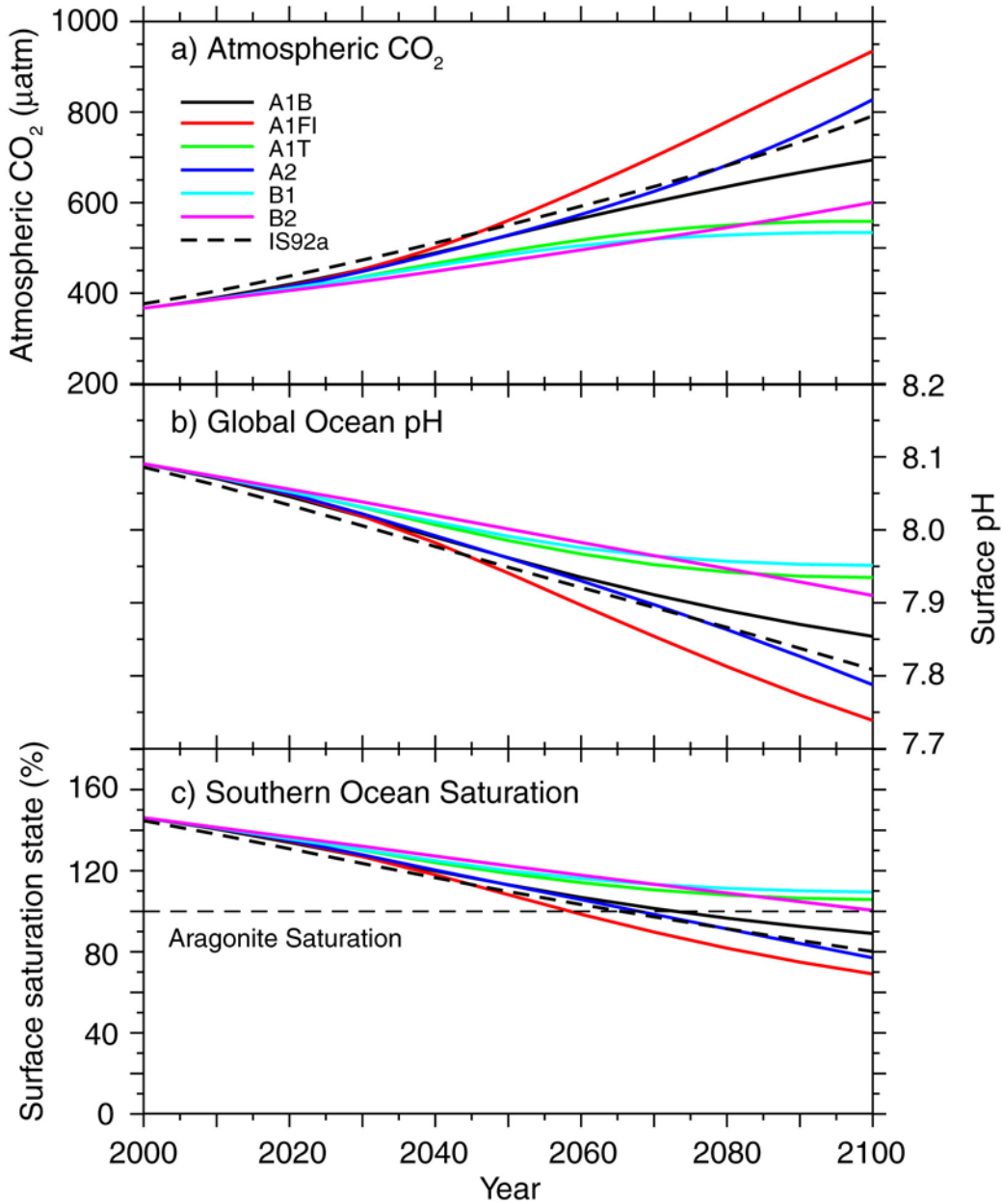
**Figure 10.22.** Projected CO<sub>2</sub> emissions leading to stabilization of atmospheric CO<sub>2</sub> concentrations at different levels and the effect of uncertainty in carbon cycle processes on calculated emissions. Panel a) shows the assumed trajectories of CO<sub>2</sub> concentration (SP scenarios) (Knutti et al., 2005); b) and c) show the implied CO<sub>2</sub> emissions, as projected with the Bern2.5CC EMIC (Joos et al., 2001; Plattner et al., 2001). The ranges given in b) for each of the SP scenarios represent effects of different model parameterizations and assumptions illustrated for scenario SP550 in panel c) (range for "CO<sub>2</sub> + climate"). The upper and lower bounds in b) are indicated by the top and bottom of the shaded areas. Alternatively, the lower bound (where hidden) is indicated by a dashed line. Panel c) illustrates emission ranges and sensitivities for scenario SP550.

1  
23  
4

5 **Figure 10.23.** Multi-model median for projected levels of saturation (in %) with respect to aragonite, a  
6 metastable form of calcium carbonate, over the 21st century from the OCMIP-2 models (adapted from Orr et  
7 al., 2005). Calcium carbonate dissolves at levels below 100%. Surface maps (left) and combined  
8 Pacific/Atlantic zonal mean sections (right) are given for scenario IS92a as averages over three time periods:  
9 2011–2030 (top), 2045–2065 (middle), and 2080–2099 (bottom). Atmospheric CO<sub>2</sub> concentrations for these  
10 three periods average 440, 570, and 730 ppm. Latitude-depth sections start in the North Pacific (at the left  
11 border), extend to the Southern Ocean Pacific section, and return through the Southern Ocean Atlantic  
12 section to the North Atlantic (right border). At 100%, waters are saturated (solid black line - the aragonite  
13 saturation horizon); values larger than 100% indicate supersaturation; values lower than 100% indicate  
14 undersaturation. The data-based (GLODAP) 1994 saturation horizon is additionally shown (solid white line)  
15 to illustrate the projected changes in the saturation horizon since present.

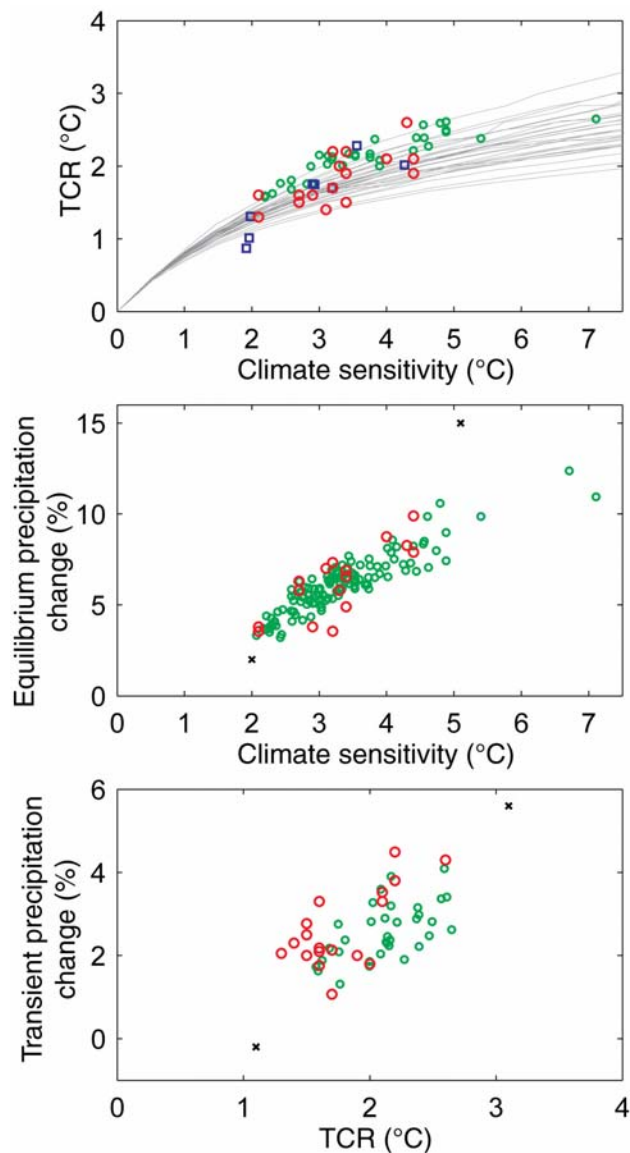
16

1  
2



3  
4  
5  
6  
7  
8  
9  
10

**Figure 10.24.** Global average surface pH changes and saturation state with respect to aragonite in the Southern Ocean under various SRES scenarios. Time series of a) atmospheric CO<sub>2</sub> for the six illustrative IPCC SRES scenarios, b) projected global average surface pH changes, and c) projected average saturation state in the Southern Ocean for the BERN2.5D EMIC (Plattner et al., 2001). The results for the SRES scenarios A1T and A2 are similar to those for the non-SRES scenarios S650 and IS92a, respectively. Modified from Orr et al. (2005).

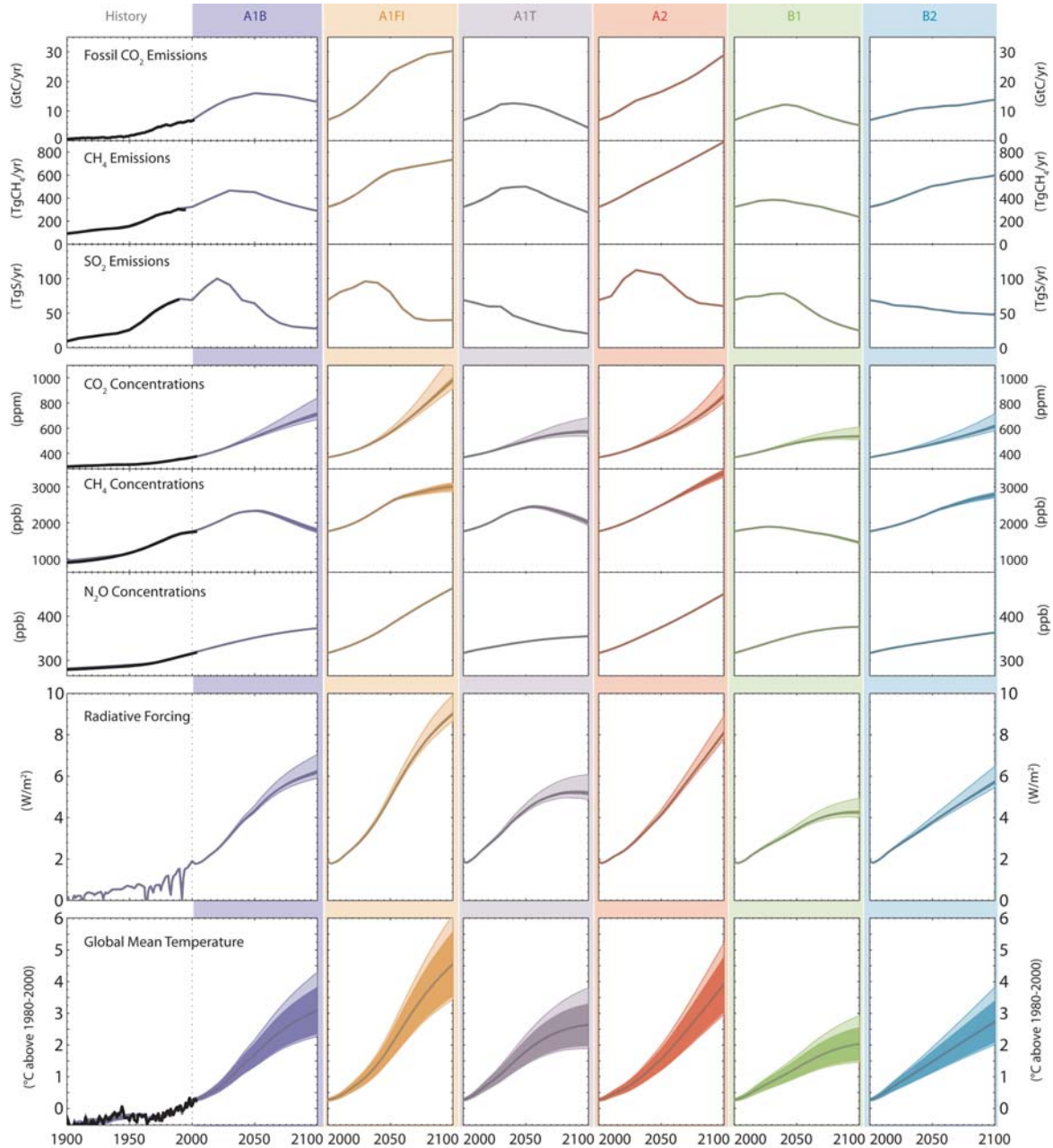
1  
2

3

4

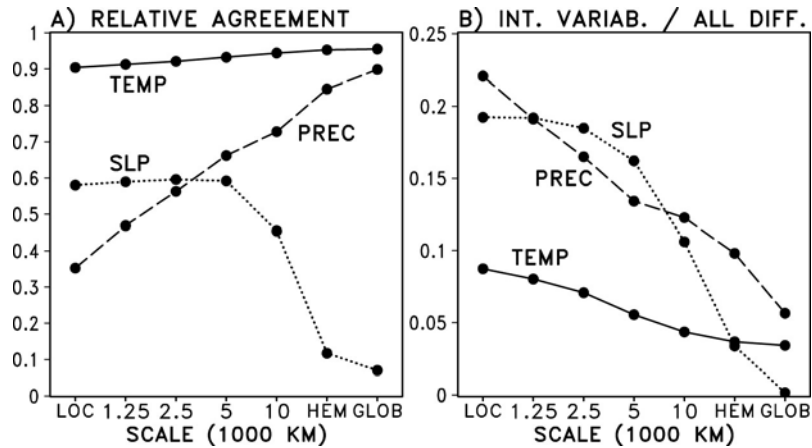
5 **Figure 10.25.** a) TCR versus equilibrium climate sensitivity for all AOGCMs (red dots), EMICs (blue dots),  
6 a perturbed physics ensemble of the HadCM3 AOGCM (green dots - an updated ensemble based on (M.  
7 Collins et al., 2006)), and from a large ensemble of the Bern2.5D EMIC (Knutti et al., 2005) using different  
8 ocean vertical diffusivities and mixing parameterizations (grey lines). b) Global mean precipitation change  
9 (%) as a function of global mean temperature change at equilibrium for doubling CO<sub>2</sub> in atmospheric GCMs  
10 coupled to a non-dynamic slab ocean (red dots all AOGCMS, green dots from a perturbed physics ensemble  
11 of the atmosphere/slab ocean version of HadCM3 (Webb et al., 2006)). c) Global mean precipitation change  
12 (in %) as a function of global mean temperature change (TCR) at the time of doubling in a transient 1%/yr  
13 CO<sub>2</sub> increase scenario, simulated by coupled AOGCMs (red) and the HadCM3 perturbed physics ensemble  
14 (green). Black crosses in b and c mark ranges covered by the IPCC TAR (2001) AOGCMs for each quantity.  
15

1  
2



3  
4  
5  
6  
7  
8  
9  
10  
11  
12  
13  
14  
15  
16  
17

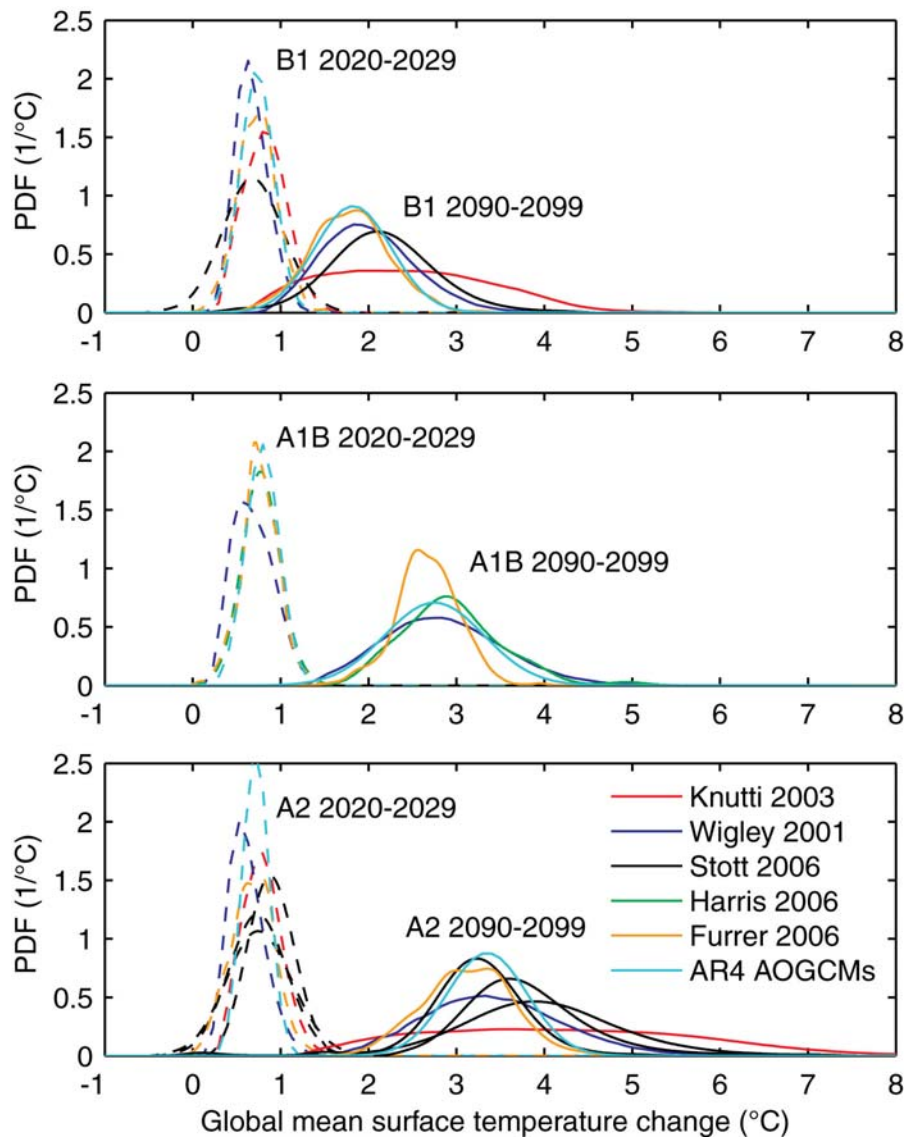
**Figure 10.26.** Fossil CO<sub>2</sub>, CH<sub>4</sub>, and SO<sub>2</sub> emissions for six illustrative SRES non-mitigation emission scenarios, their corresponding CO<sub>2</sub>, CH<sub>4</sub>, and N<sub>2</sub>O concentrations, radiative forcing and global mean temperature projections based on a simple climate model tuned to nineteen AOGCMs. The dark shaded areas in the bottom temperature panel represent the mean ±1 standard deviation for the nineteen model tunings. The lighter shaded areas depict the change in this uncertainty range, if carbon cycle feedbacks are assumed to be lower or higher than in the medium setting. Mean projections for mid carbon cycle assumptions for the six illustrative SRES scenarios are shown as thick colored lines. Historical emissions are shown for fossil and industrial CO<sub>2</sub> (Marland et al., 2005), for SO<sub>2</sub> (van Aardenne et al., 2001) and CH<sub>4</sub> ((van Aardenne et al., 2001), adjusted to (Olivier and Berdowski, 2001)). Observed CO<sub>2</sub>, CH<sub>4</sub>, and N<sub>2</sub>O concentrations are as presented in Chapter 6. Global mean temperature results from the simple climate model for anthropogenic and natural forcing compare favourably with 20th century observations as shown in the lower left panel (Folland et al., 2001; Jones et al., 2001; Jones and Moberg, 2003).

1  
23  
4

5 **Figure 10.27.** Statistics of annual mean responses to the SRES A1B scenario, for 2080–2099 relative to  
6 1980–1999, calculated from the 21 member AR4 multi model ensemble using the methodology of Räisänen  
7 (2001). Results are expressed as a function of horizontal scale (“Loc” = gridbox scale; “Hem” = hemispheric  
8 scale; “Glob” = global mean): (a) The relative agreement between ensemble members, defined as the square  
9 of the ensemble-mean response (corrected to avoid sampling bias) divided by the mean squared response of  
10 individual ensemble members; (b) The contribution of internal variability to the ensemble variance of  
11 responses. Values are shown for surface air temperature, precipitation and sea level pressure. The low  
12 agreement on SLP changes on hemispheric and global scales reflects problems with the conservation of total  
13 atmospheric mass in some of the models; however this has no practical significance because SLP changes on  
14 these scales are extremely small.

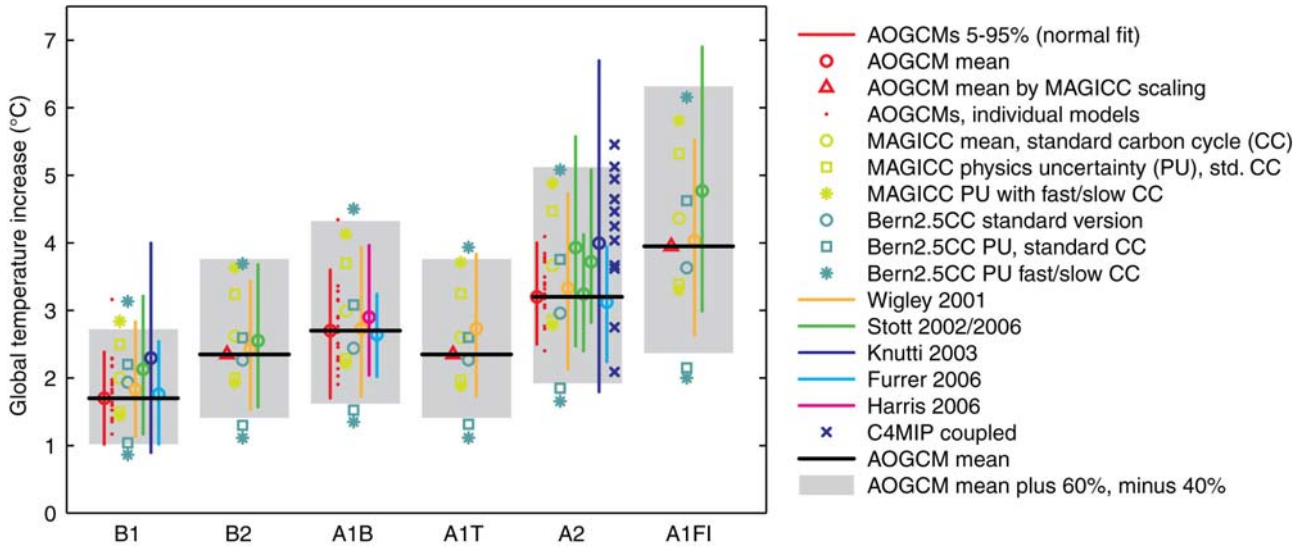
15

1  
2  
3

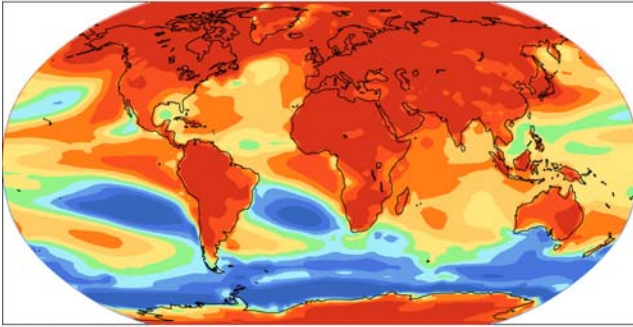
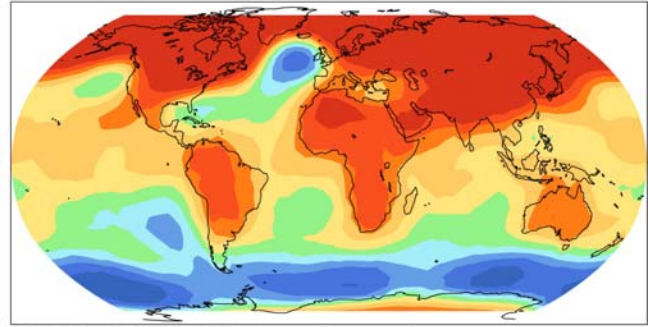
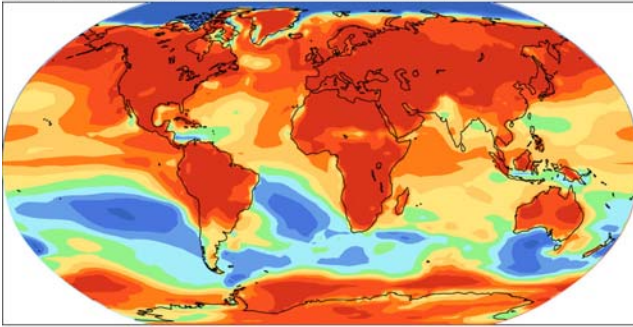
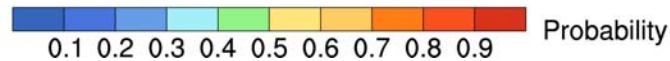
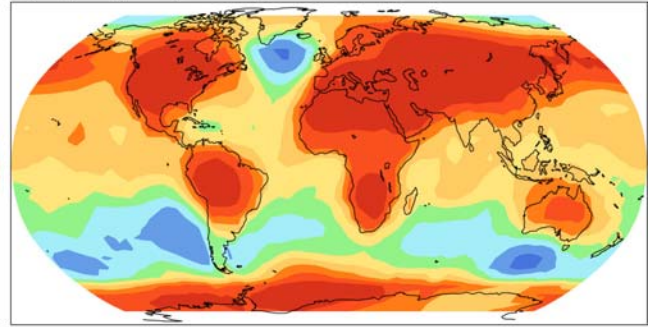


4  
5  
6  
7  
8  
9  
10

**Figure 10.28.** Probability density functions from different studies for global mean temperature change for the SRES scenarios B1, A1B and A2 and for the decades 2020–2029 and 2090–2099 relative to the 1980–1999 average (Wigley and Raper, 2001; Knutti et al., 2002; Furrer et al., 2006; Harris et al., 2006; Stott et al., 2006b). A normal distribution fitted to the multi-model ensemble is given for comparison.

1  
23  
4  
5  
6  
7  
8  
9  
10  
11  
12  
13  
14  
15  
16  
17  
18  
19  
20  
21

**Figure 10.29.** Projections and uncertainties for global mean temperature increase in 2090–2099 (relative to the 1980–1999 average) for the six SRES marker scenarios. AOGCM mean, and the range of the mean minus 40% to plus 60% are shown as black horizontal solid lines and grey bars, respectively. For comparison, results are given for the individual models (black dots) of the multi-model AOGCM ensemble for B1, A1B and A2, with a mean and 5–95% range (red line and circle) from a fitted normal distribution. AOGCM mean estimates for B2, A1T and A1FI (red triangles) are obtained by scaling the A1B AOGCM mean with ratios obtained from the SCM (see text). The mean (light green circle) and one standard deviation (light green square) of the MAGICC SCM tuned to all AOGCMs (representing the physics uncertainty) are shown for standard carbon cycle settings, as well as for a slow and fast carbon cycle assumption (light green stars). Similarly, results from the Bern2.5CC EMIC are shown for standard carbon cycle settings and for climate sensitivities of 3.2°C (AOGCM average, dark green circle), 1.5 and 4.5°C (dark green squares). High climate sensitivity/slow carbon cycle as well as low climate sensitivity/fast carbon cycle combinations are shown as dark green stars. 5-95% ranges (vertical lines) and medians (circles) are shown from probabilistic methods (Wigley and Raper, 2001; Stott and Kettleborough, 2002; Knutti et al., 2003; Furrer et al., 2006; Harris et al., 2006; Stott et al., 2006b). Individual model results are given for the C4MIP models (blue crosses, see Figure 10.20).

1  
2a)  $P[\Delta T(\text{DJF}) > 2^\circ\text{C}]$ , perturbed physicsb)  $P[\Delta T(\text{DJF}) > 2^\circ\text{C}]$ , multi-modelc)  $P[\Delta T(\text{JJA}) > 2^\circ\text{C}]$ , perturbed physicsd)  $P[\Delta T(\text{JJA}) > 2^\circ\text{C}]$ , multi-model

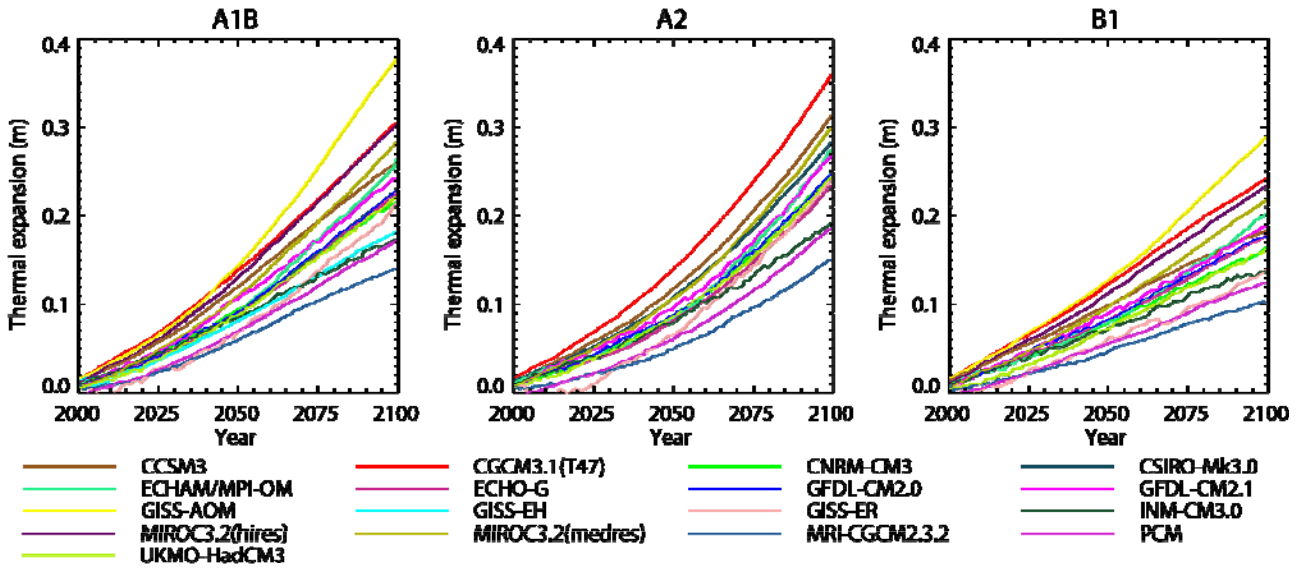
3

4

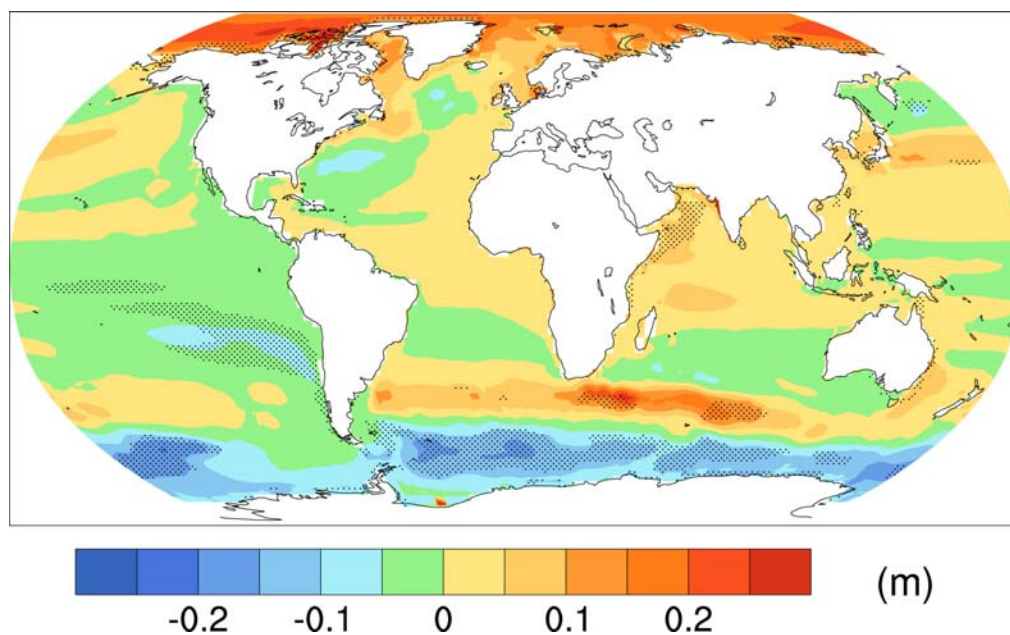
5 **Figure 10.30.** Estimated probabilities for a mean surface temperature change exceeding  $2^\circ\text{C}$  under the SRES  
 6 A1B scenario, for 2080–2099 relative to 1980–1999. Results obtained from a perturbed physics ensemble of  
 7 a single model (panels a and c), based on Harris et al. (2006), are compared against results from the AR4  
 8 multi model ensemble (panels b and d), based on Furrer et al. (2006), for December-February (DJF, panels a  
 9 and b) and June-August (JJA, panels c and d).

10

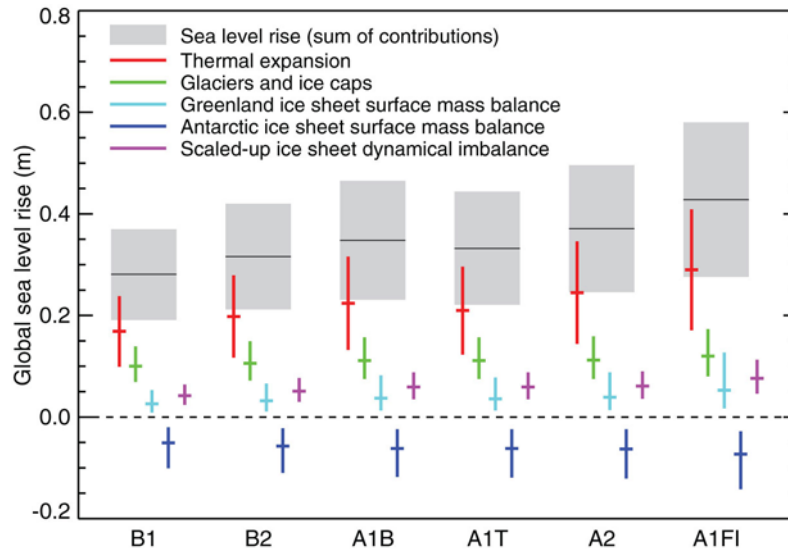
1  
2  
3  
4  
5  
6  
7



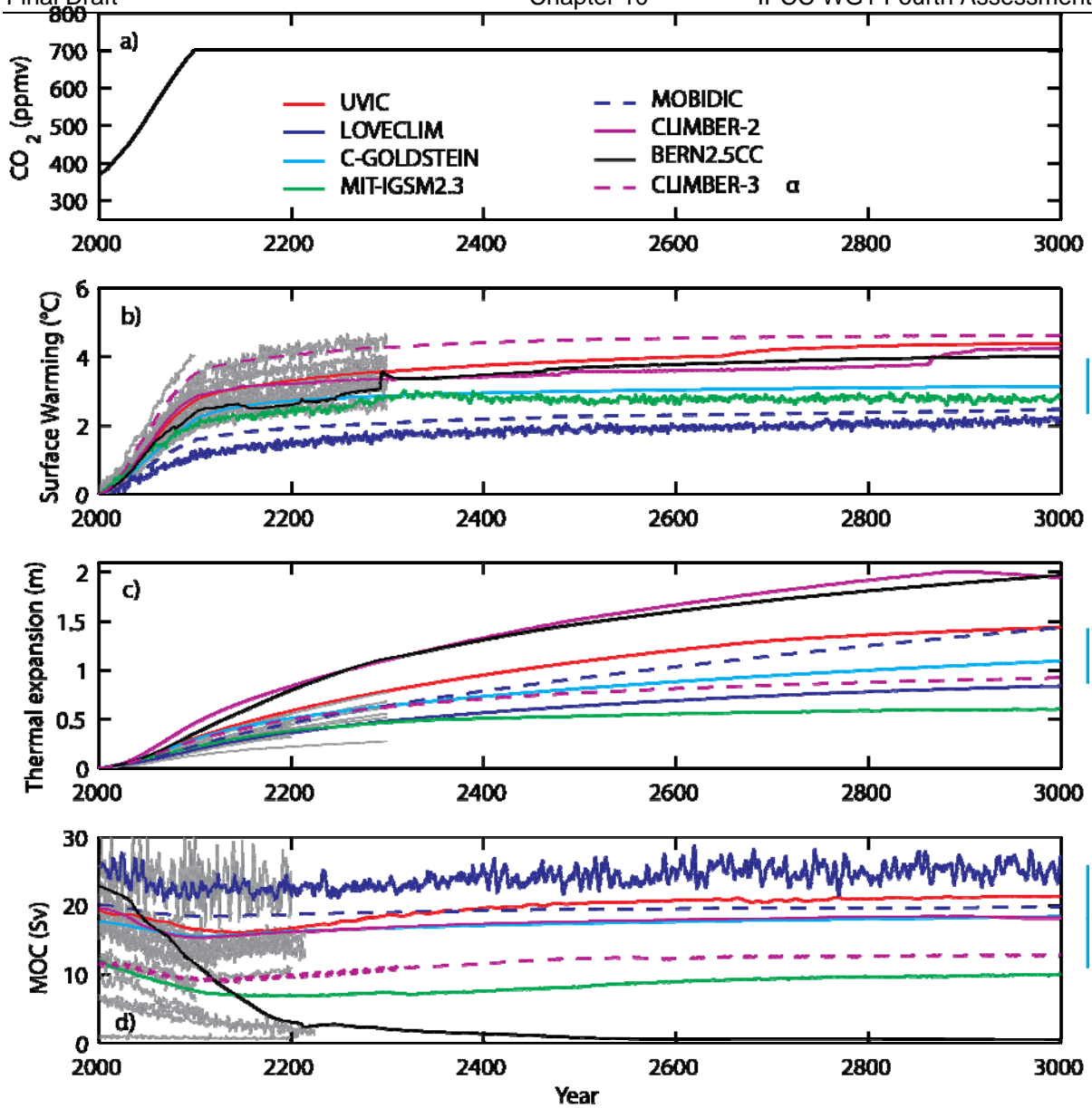
**Figure 10.31.** Projected global average sea level rise (m) due to thermal expansion during the 21st century relative to 1980–1999 under SRES scenarios A1B, A2 and B1.

1  
23  
4  
5  
6  
7  
8  
9  
10

**Figure 10.32.** Local sea level change (m) due to ocean density and circulation change relative to the global average (i.e., positive values indicate greater local sea level change than global) during the 21st century, calculated as the difference between averages for 2080–2099 and 1980–1999 under SRES scenario A1B, as an ensemble mean over 16 AOGCMs. Stippling denotes regions where the multi-model ensemble mean divided by the multi-model standard deviation exceeds 1.0 (in magnitude).

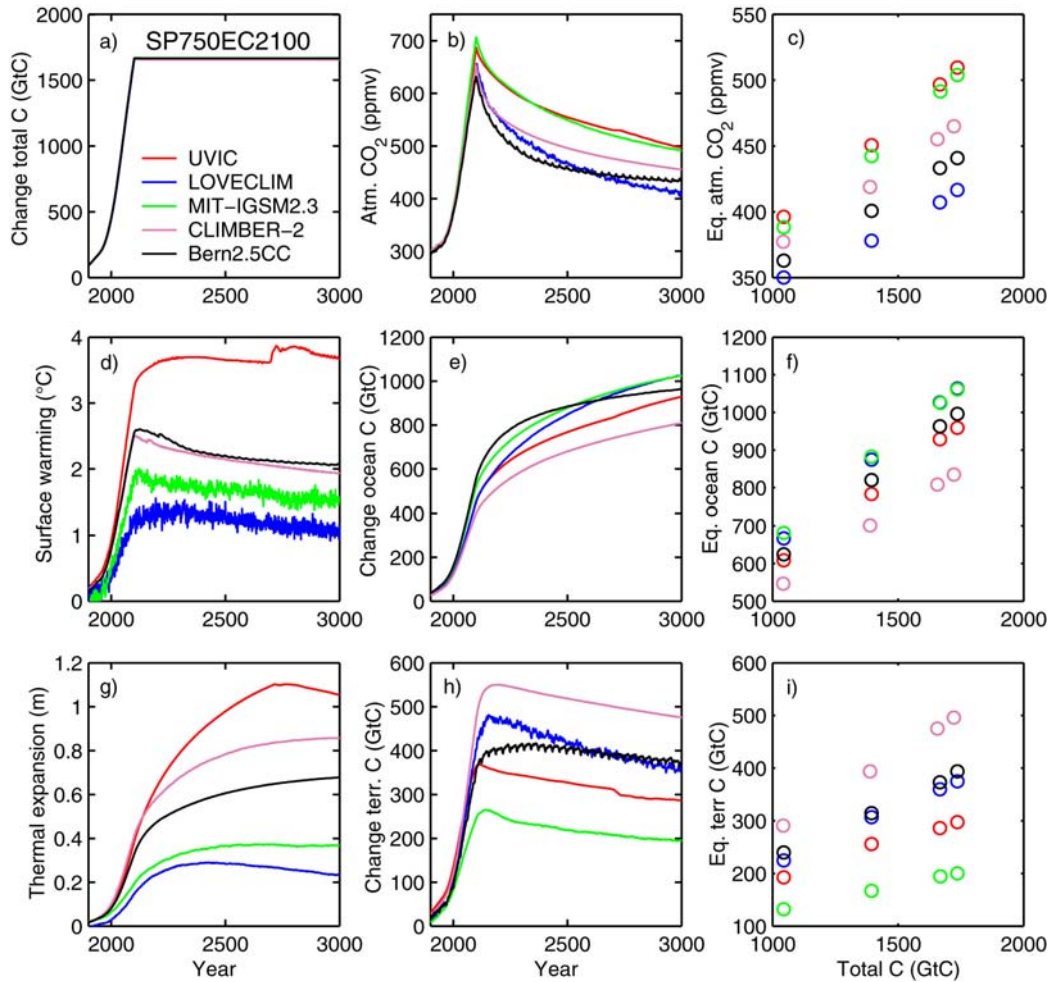
1  
23  
4  
5  
6  
7  
8  
9  
10  
11  
12  
13

**Figure 10.33.** Projection and uncertainties (5–95% ranges) for global average sea level rise and its components in 2090–2099 (relative to 1980–1999) for the six SRES marker scenarios. The projected sea level rise assumes that the part of the present-day ice sheet mass imbalance that is due to recent acceleration of ice-flow will persist unchanged. It does not include the contribution shown from scaled-up ice sheet discharge, which is an alternative possibility. It is also possible that the present imbalance might be transient, in which case the projected sea level rise is reduced by 0.02 m. We emphasise that we cannot assess the likelihood of any of these three alternatives, which are presented as illustrative. The state of understanding prevents a best estimate from being made.



1  
 2  
 3  
 4 **Figure 10.34.** a) atmospheric CO<sub>2</sub>, b) global mean surface warming, c) sea level rise from thermal expansion  
 5 and d) Atlantic meridional overturning circulation calculated by eight EMICs for the SRES A1B scenario  
 6 and stable radiative forcing after 2100, showing long-term commitment after stabilization. Coloured lines are  
 7 results from EMICs, grey lines indicate AOGCM results where available for comparison. Anomalies in b  
 8 and c are given relative to the year 2000. Vertical bars indicate plus/minus two standard deviation  
 9 uncertainties due to ocean parameter perturbations in the C-Goldstein model. The MOC shuts down in the  
 10 Bern model, leading to an additional contribution to sea level rise. Individual EMICs treat the effect from  
 11 non-CO<sub>2</sub> greenhouse gases and the direct and indirect aerosol effects on radiative forcing differently. Despite  
 12 similar atmospheric CO<sub>2</sub> concentrations, radiative forcing among EMICs can thus differ within the  
 13 uncertainty ranges currently available for present-day radiative forcing (see Chapter 2).  
 14

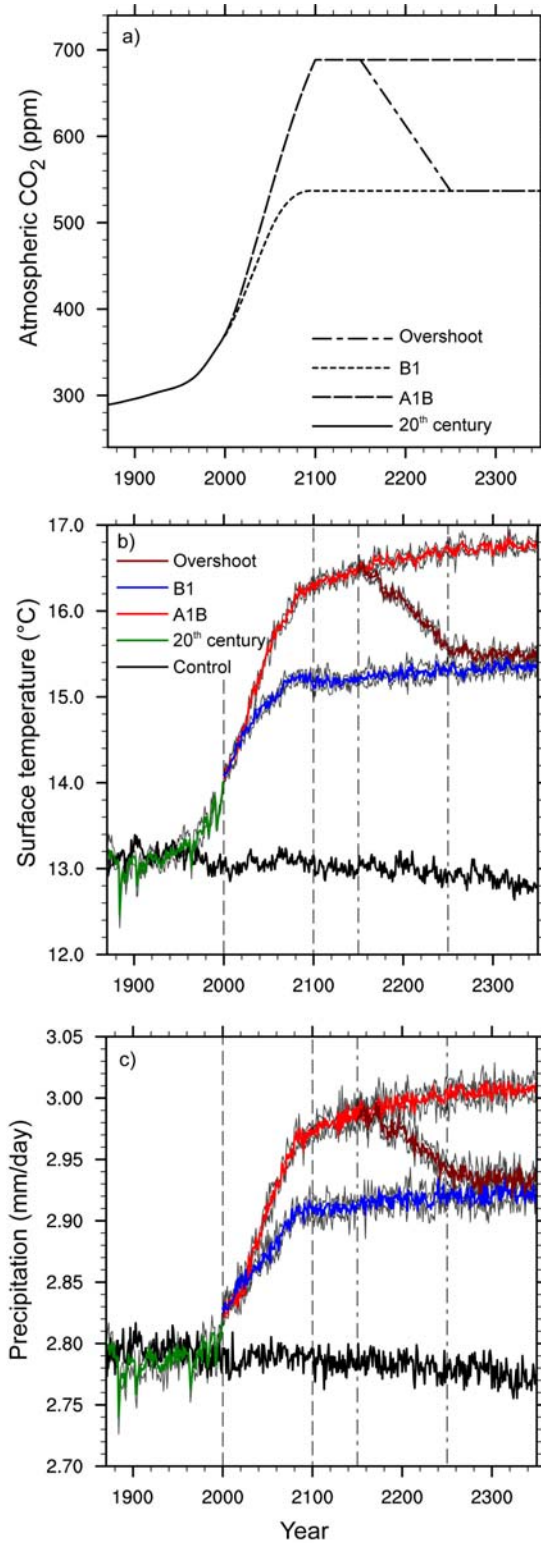
1  
2



3  
4  
5  
6  
7  
8  
9  
10  
11  
12

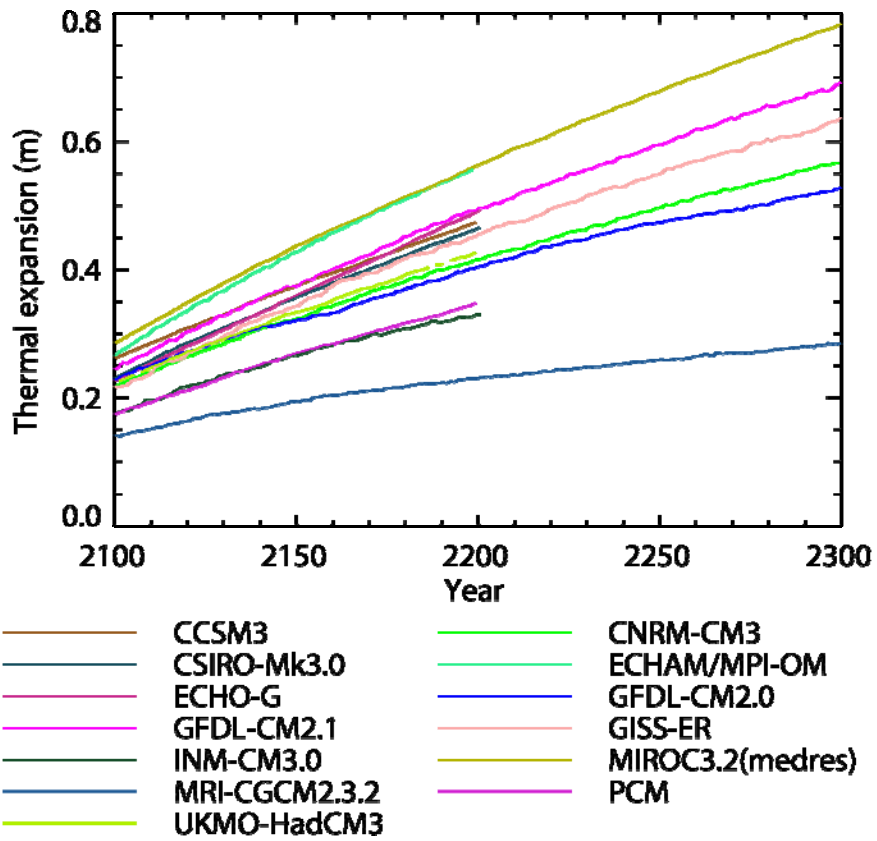
**Figure 10.35.** Changes in carbon inventories and climate response relative to preindustrial for five different intermediate complexity models, in a scenario where emissions follow a pathway leading to stabilization of atmospheric CO<sub>2</sub> at 750 ppmv, but before reaching this target, emissions are reduced to zero instantly at year 2100. a) change in total carbon, b) atmospheric CO<sub>2</sub>, d) change in surface temperature, e) change in ocean carbon, g) sea level rise from thermal expansion, h) change in terrestrial carbon. Right column: c) atmospheric CO<sub>2</sub>, f) oceanic and i) terrestrial carbon uptake at year 3000 relative to preindustrial for several emission scenarios of similar shape but with different total carbon emissions.

1  
2



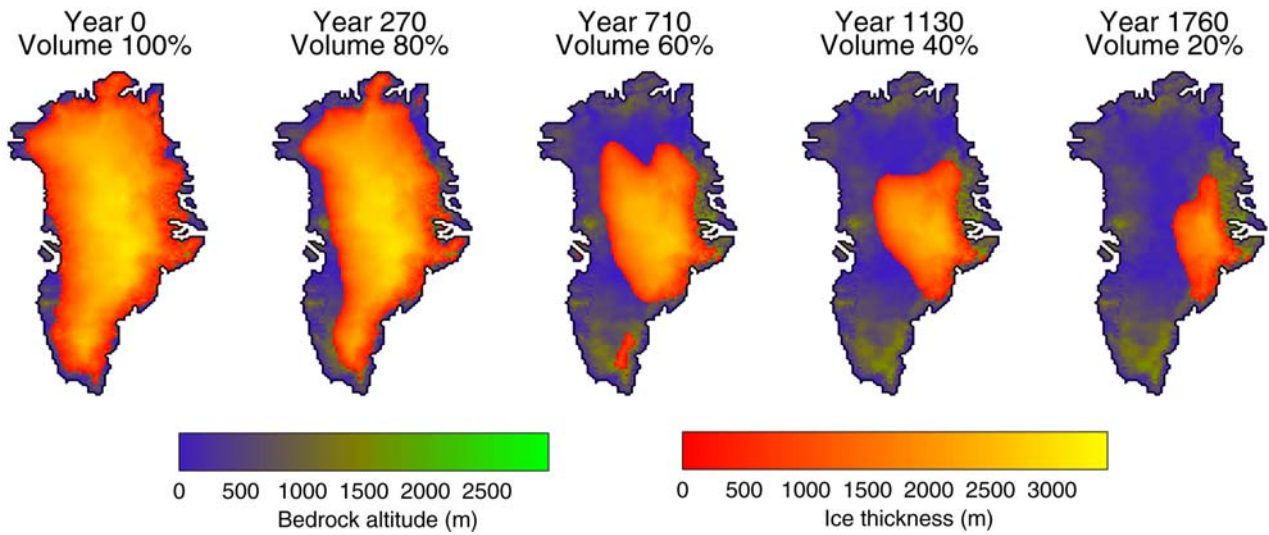
3  
4  
5  
6  
7

**Figure 10.36.** a) Atmospheric CO<sub>2</sub> concentrations for several experiments simulated with an AOGCM. b) globally averaged surface air temperatures for the overshoot scenario and the A1B and B1 experiments; c) same but for globally averaged precipitation rate. Modified from Yoshida et al. (2005).

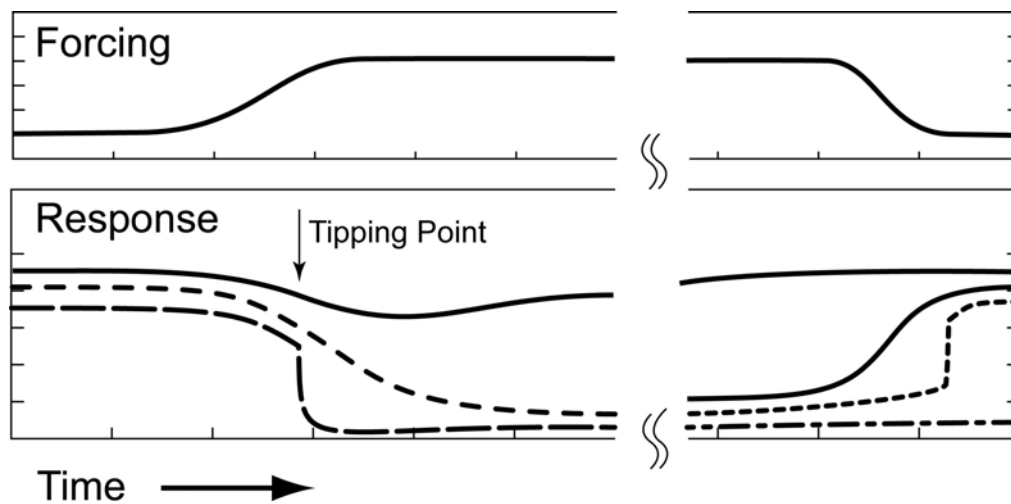


1  
2  
3  
4  
5

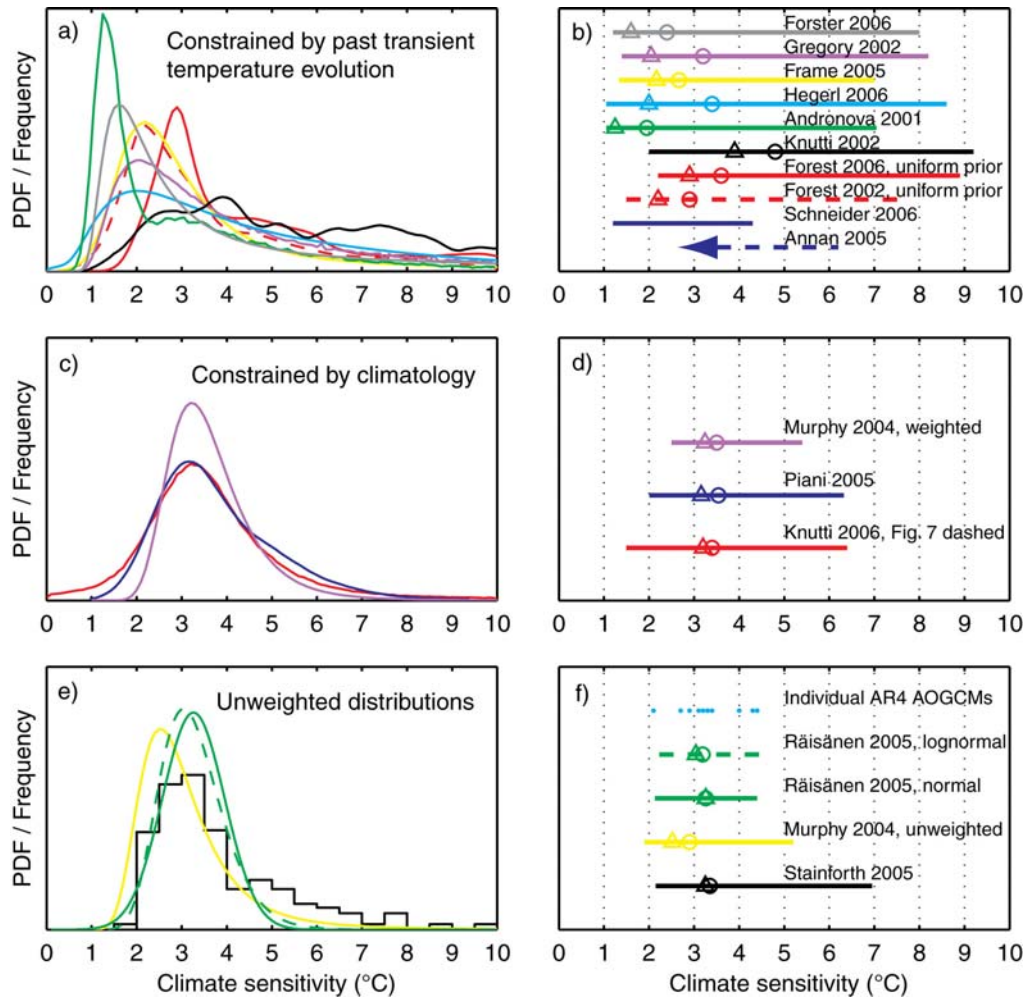
**Figure 10.37.** Globally averaged sea level rise from thermal expansion relative to year 1980–1999 for the A1B commitment experiment calculated from AOGCMs.

1  
23  
4  
5  
6  
7  
8

**Figure 10.38.** Evolution of Greenland surface elevation and ice sheet volume versus time in the experiment of Ridley et al. (2005) with the HadCM3 AOGCM coupled to the Greenland ice sheet model of Huybrechts and De Wolde (1999) under a climate of constant four times preindustrial CO<sub>2</sub>.

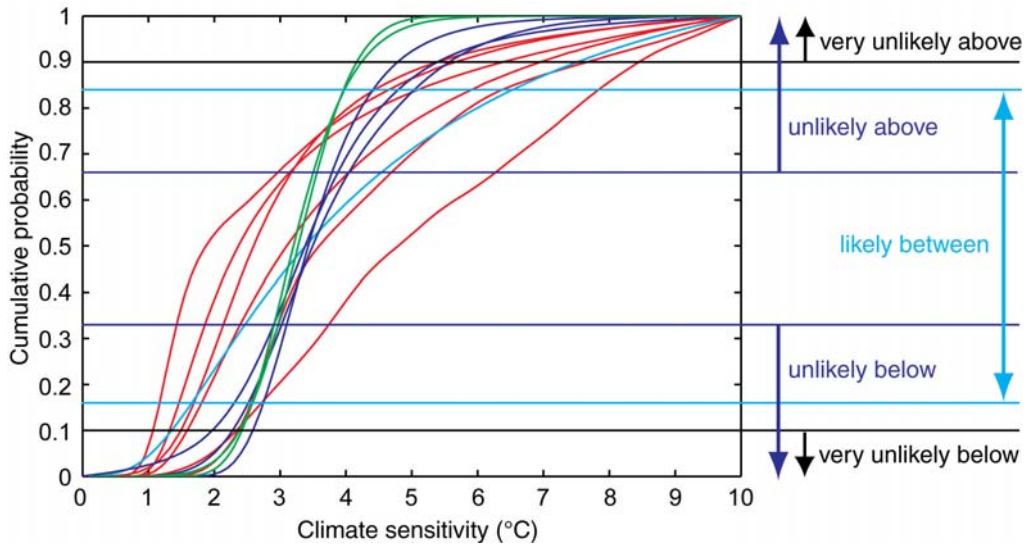
1  
2  
34  
5  
6  
7  
8  
9  
10  
11  
12  
13  
14  
15  
16  
17

**Box 10.1, Figure 1.** Schematic illustration of various responses of a climate variable to forcing. The forcing (top panels) reaches a new stable level (left part of figure), and later approaches the original level on very long time scales (right part of the figure). The response of the climate variable (bottom panels) can be smooth (solid line) or cross a tipping point inducing a transition to a structurally different state (dashed lines). That transition can be rapid (abrupt change, long-dashed), or gradual (short-dashed), but is usually dictated by the internal dynamics of the climate system rather than the forcing. The long-term behaviour (right panel) also exhibits different possibilities. Changes can be irreversible (dash-dotted) with the system settling at a different, stable state, or reversible (solid, dotted) when the forcing is set back to its original value. In the latter case, the transition can, again, be gradual or abrupt. One example for the illustration, but not limited to, is the response of the Atlantic meridional overturning circulation to a gradual change in radiative forcing.

1  
23  
4  
5  
6  
7  
8  
9  
10  
11  
12  
13

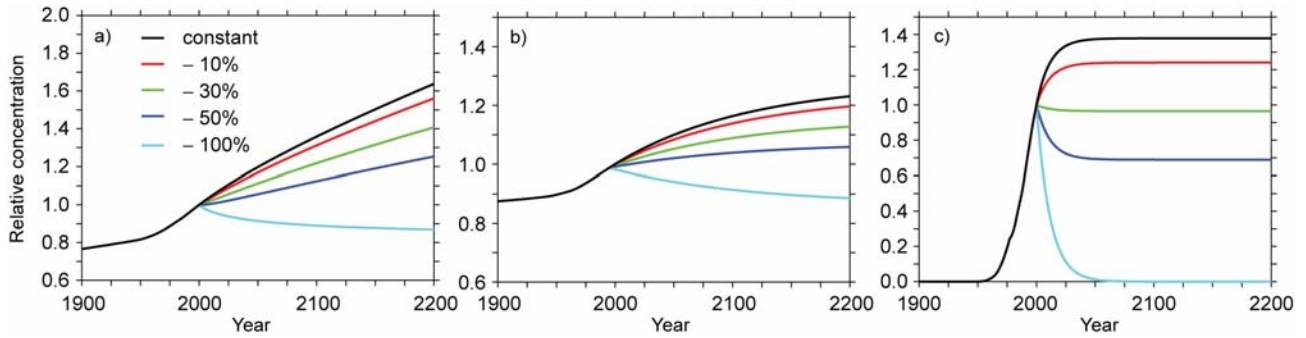
**Box 10.2, Figure 1.** a) PDFs or frequency distributions constrained by the transient evolution of the atmospheric temperature, radiative forcing and ocean heat uptake, b) as in panel a) but 5–95% ranges, medians (circles) and maximum probabilities (triangles), c/d) same but using constraints from present-day climatology, e/f) unweighted or fitted distributions from different models or from perturbing parameters in a single model. Distributions in panel e/f should not be interpreted as PDFs. See Chapter 9, text, Figure 9.20 and Table 9.3 for details. Note that Annan et al. (2005b) only provide an upper but no lower bound. All PDFs are truncated at 10°C for consistency, some are shown for different prior distributions than in the original studies, ranges may differ from numbers reported in individual studies.

1



2  
3  
4  
5  
6  
7  
8  
9  
10

**Box 10.2, Figure 2.** Individual cumulative distributions of climate sensitivity from the observed 20th century warming (red), model climatology (blue) and proxy evidence (cyan), taken from Box 10.2, Figure 1a/c (except LGM studies and Forest et al. (2002) which is superseded by Forest et al. (2006)) and cumulative distributions fitted to the AOGCMs climate sensitivities (green) from Box 10.2, Figure 1e. Horizontal lines and arrows mark the edges of the likelihood estimates according to IPCC guidelines.

1  
23  
4

5 **FAQ 10.3, Figure 1.** a) Simulated changes in atmospheric CO<sub>2</sub> concentration relative to the present-day for  
6 emissions stabilized at the current level (black), or at 10% (red), 30% (green), 50% (dark blue), and 100%  
7 (light blue) lower than the current level; b) same for a trace gas with a life time of 120 years, driven by  
8 natural and anthropogenic fluxes; c) same for a trace gas with a life time of 12 years, driven by only  
9 anthropogenic fluxes.

10

11